THESIS FOR THE DEGREE OF DOCTOR OF PHILOSOPHY
IN
THERMO AND FLUID DYNAMICS

Temporally gated imaging for investigation of atomizing sprays

MATTIAS RAHM

Department of Applied Mechanics
CHALMERS UNIVERSITY OF TECHNOLOGY
Göteborg, Sweden 2016

Temporally gated imaging for investigation of atomizing sprays
MATTIAS RAHM
ISBN 978-91-7597-332-6

Doktorsavhandlingar vid Chalmers tekniska högskola
Ny serie nr 4013
ISSN 0346-718X

Department of Applied Mechanics
Chalmers University of Technology
SE-412 96 Göteborg, Sweden
Phone: +46 (0)31-772 10 00

Printed by Chalmers Reproservice
Göteborg, Sweden, 2016

Temporally gated imaging for investigation of atomizing sprays

MATTIAS RAHM
Department of Applied Mechanics
Chalmers University of Technology

ABSTRACT

Fuel sprays play an important role in the combustion process of modern compression ignition engines, but their dynamics are not well understood. This thesis focuses on time-gated imaging techniques as a means to study the optically dense spray formation region of these atomizing sprays.

Initially, the performance of two ballistic imaging setups previously used in spray investigations was investigated. The investigation showed that the simpler of the two setups ($2f$) was less affected by changes in the time-gate setup, and was more robust to component misalignment. The $2f$ setup is therefore often preferable for time-gated spray investigations. Then, the ballistic imaging system was further developed with the use of three synchronized regenerative laser amplifiers. This system allowed three time-gated images with user defined inter-frame spacing to be generated. Based on these three images, two-dimensional acceleration data of larger liquid structures in the spray formation region were obtained. Such acceleration data can be used in the development of predictive computational spray codes.

Next, ballistic imaging was used to study fuel sprays at elevated pressures and temperatures. This was the first time ballistic imaging was applied to sprays at engine-relevant conditions. The ambient conditions were varied and changes in the liquid/gas interfaces in the spray formation region were studied. It was shown that especially for single-component fuels the liquid-gas interfaces exhibited a significant change, which mostly correlated with the thermodynamic properties of the fuel. These findings contribute to the ongoing discussion regarding the potential transient supercriticality of fuel sprays in modern direct injection combustion engines. The investigation of the fuel sprays further showed

that there is a need for a technique that provides depth-resolved data from the spray formation region. To this end, we developed a new approach termed time-gated sectioning. This setup captures backscattered light from the spray formation region, and was successfully able to generate a depth-resolution of $\sim$0.3 mm.

Collectively, the work presented in this thesis advances the use of time-gated imaging methods for spray investigations.

Keywords: Sprays, Imaging through turbid media, Optical Kerr effect, Ultrafast lasers, Ballistic imaging, Velocimetry, Time-gated sectioning.

Acknowledgments

First of all, I would like to thank my supervisor Mark Linne for giving me the opportunity to perform this work. Your encouragement, as well as all your knowledge and experience in physics and engineering, has been invaluable. Many thanks also to my co-advisors David Sedarsky and Mats Andersson for your help and input. Furthermore, I want to direct a big thank you to my fellow PhD students Zachary Falgout and Zhenkan Wang for all your work and help. Thanks for creating a positive and easy-going atmosphere in the lab. Megan Paciaroni, you taught me how to work with lasers and optics. I am very grateful for your help and support.

The research engineers deserve a big acknowledgement for their help regarding the projects. Patrik and Daniel, although I may not completely share your devotion to the outer space, I have enjoyed all of our discussions. Moreover, I would like to express my gratitude to the whole Division of Combustion; I have really appreciated to work here. A special thank you is directed to Amirreza Movaghar, Anders Johansson, and Rickard "pajsarn" Arvidsson, for creating a cheerful office atmosphere.

Many thanks also to my family, with its branches on the East coast, West coast, and in Norway, for all your support. Finally, Amanda, Ingrid, and Edith, you are the best, and I am so grateful for having you in my life. Without you, this would not have been possible.

List of publications

This thesis is principally based on the following publications, referred to in the text by their Roman numerals:

I. **M. Rahm**, M. Paciaroni, Z. Wang, D. Sedarsky, and M. Linne, "Evaluation of optical arrangements for ballistic imaging in sprays", Optics Express **23**, 22444-22462 (2015).

II. D. Sedarsky, **M. Rahm**, and M. Linne, "Visualization of acceleration in multiphase fluid interactions", Optics Letters **41**, 1404-1407 (2016).

III. Z. Falgout, **M. Rahm**, Z. Wang, and M. Linne, "Evidence for supercritical mixing layers in the ECN Spray A", Proceedings of the Combustion Institute **35**, 1579-1586 (2015).

IV. Z. Falgout, **M. Rahm**, D. Sedarsky, and M. Linne, "Gas/fuel jet interfaces under high pressures and temperatures", Fuel **168**, 14-21 (2016).

V. **M. Rahm**, Z. Falgout, D. Sedarsky, and M. Linne, "Optical sectioning for measurements in transient sprays", Optics Express **24**, 4610-4621 (2016).

Contents

Nomenclature

BBO	**β-Barium Borate**
BI	**Ballistic imaging**
c	**Speed of light in vacuum**
CTF	**Contrast transfer function**
DICI	**Direct injection compression ignition**
ECN	**Engine Combustion Network**
FWHM	**Full width at half maximum**
HCSI	**Homogenous charge spark ignition**
ICV	**Image correlation velocimetry**
IR	**Infrared**
lp/mm	**Line-pair/millimeter**
OCT	**Optical coherence tomography**
OD	**Optical depth**
OKE	**Optical Kerr effect**
OPL	**Optical path length**
PDA	**Phase doppler anemometry**
PDS	**Planar droplet sizing**
PS	**Polystyrene**
SHG	**Second harmonic generation**
SLIPI	**Structured laser illumination planar imaging**
SPDI	**Spectral polarization difference imaging**
TGS	**Time-gated sectioning**

UV **Ultraviolet**

List of Figures

Chapter 1

Introduction

It is hard to overestimate the importance of liquid fuels, and more specifically fossil fuels, in the transportation sector of today [1]. Liquid fuels are in use because they have significantly higher volumetric energy density than fuels in other phases and technologies relying on other sources of energy [2, 3]. However, acknowledging the climate effects resulting from the continued consumption of fossil resources, there is an ambition to reduce the world's dependence on petroleum products [4]. To further this goal, resources are invested in research, development, and utilization of liquid fuels from renewable sources to replace the fossil fuels in the context of transportation. Consequently, liquid fuels and internal combustion engines will likely be an important part of the transportation industry for years to come. Therefore, further research is needed to improve engine efficiency and reduce the generation of harmful emissions.

In combustion engines, the chemical energy in the fuel is most often released through gas-phase oxidation with ambient oxygen. For this process to be completed in a single engine cycle there is a need to vaporize and mix the initially liquid fuel with the ambient gas in a fast and efficient way. In an internal combustion engine, this is done by conversion of the contiguous liquid

into a dispersed spray by injecting it into the ambient gas through a nozzle. Transforming the contiguous liquid fuel into a collection of small drops effectively increases the surface/mass ratio of the fuel. Since evaporation takes place at the liquid/gas interfaces, the speed of the process is significantly increased. In homogenous charge spark ignition (HCSI) engines, the fuel is injected into the ambient gas prior to the ignition event. Consequently, the fuel has time to vaporize and mix with the ambient gas, producing a homogenous, combustible mixture. In the case of direct injection compression ignition (DICI) engines, or Diesel-like engines, on the other hand, combustion is mixing controlled (see *e.g.* [5]). Here the rate of combustion is controlled by the vaporization and mixing of fuel with the combustion chamber gas. That is, the spray plays an important role in the subsequent combustion. Detailed understanding of the processes involved during fuel injection is vital for prediction and optimization of DICI engines in order to increase combustion efficiency and reduce the production of harmful emissions.

The current ability to understand and predict the mechanics of spray formation and sprays is, however, limited. Sprays are turbulent multiphase flows, which are difficult to investigate both from the computational and experimental perspective. To avoid intrusive measurement techniques, which affect the flow field of the spray itself, experimental research in this field relies heavily on radiation-based techniques. Electromagnetic radiation covering the spectrum from infrared (IR), through optical wavelengths, down to hard X-rays is used in various applications.

Near the nozzle, in the spray formation region, the conditions are very challenging for optical techniques. Drops and ligaments are being stripped from the larger fluid structures, and form a dense multiphase flow which effectively scatters light in the visible and IR spectrum. This scattering tends to shield the interior of the spray formation region, making imaging of the fluid dynamics here both difficult and prone to corruption. Consequently, diagnostic techniques designed to probe this region all utilize schemes to mitigate this light scattering.

This thesis is concerned with further development of time-gated imaging techniques designed to probe the spray formation region of the atomizing sprays of modern DICI engines. To this end, work on both ballistic imaging (BI) and time-gated sectioning (TGS) are presented. BI is a line-of-sight shadow-imaging technique designed to mitigate the effects light scattering from the drop cloud surrounding the spray formation region. In the context of spray research, TGS is a new approach based on backscattered light with the potential of extracting a backscattered light signal from a well-defined planar section within the probed region.

The structure of this thesis will be as follows: Chapter 1 gives an introduction to the thesis. Chapter 2 covers spray breakup, light scattering from drops, and examples of current techniques used to probe the spray formation region. Chapter 3 contains an in-depth discussion of the ballistic imaging technique, and in Chapter 4 time-gated sectioning is presented. In Chapter 5 the results from the attached papers together with recent non-published findings are presented.

Chapter 2

Spray formation region

2.1 Background

A spray can be defined as a dispersion of small drops moving through an ambient gas. In a DICI engine context, the spray is created by using a large pressure difference across the injector to push the liquid fuel through a small diameter orifice (called a pressure-atomized injector). The flow through the nozzle is complex with high velocities and, depending on the detailed nozzle geometry, the possibility for cavitation [6, 7]. The conventional understanding is that in DICI engines, the fuel and air mix in thermodynamically subcritical states. Being in such a state implies that the fuel can be described by two different phases (liquid and vapor), and that surface tension forces play a significant role in the fuel-gas interaction. The flow that exits the nozzle is complex, with larger contiguous liquid structures breaking up and shedding droplets both due to turbulence in the liquid, and to aerodynamic shear due to the relative motion and momentum exchange with the ambient gas. This process of primary breakup continues downstream until all liquid is dispersed into drops. At this location, the flow can be called a spray in accordance with the definition above. Here

the spray continues to evolve; the density decreases due to the increased cross-sectional area of the spray, and the drops break up further via secondary breakup processes.

In line with this terminology, the region between the nozzle and the start of the spray region is called the spray formation region. The flow that exits the nozzle is not optically dense, but over a short distance, within micrometers [8], a very dense cloud of drops can develop. Thus, the spray formation region consists of larger liquid structures in various stages of atomization submerged in a dense cloud of drops. The process, starting with the intra-nozzle flow and developing a spray is not fully understood. Consequently, there is a lack of predictive computational models that can be used in injector and engine development. Among other things, the detailed interactions between turbulence, shear, and cavitation are not known.

Recently the paradigm that liquid fuel sprays in Diesel engines are in a thermodynamically subcritical state governed by the atomization mechanisms of two-phase flows has been questioned. It has been proposed that during certain engine loads, the pressure and temperature in the combustion chamber can exceed the critical point, thus placing the jet in the spray formation region in a supercritical regime [9–12]. In such a thermodynamic state, the mechanisms governing fuel/air mixing are different from the ones controlling subcritical two-phase mixing. The surface tension would be significantly reduced, and the liquid/gas interfaces, where ligaments and drops would be shed, would be replaced by a thickened turbulent mixing layer. Therefore, turbulent diffusive mixing would dominate. This idea is, however, not fully accepted. Among other things, it has been questioned if this potential single-phase would be thermodynamically stable under the conditions that occur [13, 14]. It is still an open question whether the transition to a supercritical state can take place during relevant engine loads, and if so, if it can happen with multicomponent Diesel blends and not only with single-component fuels. Paper III and Paper IV of this thesis are concerned with investigations of these proposed phase transitions. Here BI and non-gated shadow-imaging are used to evaluate changes in the spray

structure due to changes in ambient conditions.

Experimentally the spray formation region is challenged by a number of factors. Experimentation at realistic engine conditions requires specialized facilities (*e.g.* optically accessible engines or high pressure/high temperature vessels with appropriate means of experimental access). The high velocities involved impose stringent requirements on temporal resolution if suppression of averaging due to motion blur effects is needed. A dense droplet cloud also contributes to experimental difficulties. Light will interact with the droplets, and this interaction can shield larger fluid structures undergoing breakup from being observed directly. The three dimensional nature of the flow imposes challenges since experimental approaches are often point-wise or two-dimensional.

2.2 Light interaction with sprays

2.2.1 Single scattering

When light is incident on the flow in the spray formation region it will scatter from the drops and, close to the liquid core, from ligaments. Detailed descriptions of the physics governing this scattering are in general very complex. Therefore, the discussion is often simplified by assuming spherical symmetry of the scattering objects. This assumption also serves as a first order approximation to the scattering from non-spherical objects. This simplification will be the basis for the discussion below.

The nature of the light scattering depends on the difference in refractive index between the drop and the ambient gas, and on the difference in length scales between the drop and the wavelength of the radiation. The length scale difference can be quantified by the size parameter of the interaction, α [15]:

$$\alpha = \frac{2\pi d}{\lambda}. \tag{2.1}$$

In Eq. 2.1, d is the drop diameter, and λ the wavelength of the radiation in

the ambient medium. Depending on the size parameter, the scattering can be divided into three different regimes. If $\alpha \ll 1$, the scattering takes place in what is called the Rayleigh regime, and if α is on the order of 1, it takes place in the Mie regime. When the size parameter becomes very large ($\alpha \gg 1$), the scattered intensity can be approximated with classical geometrical optics ray tracing approaches. If one assumes for example a wavelength of 800 nm (center wavelength of the pulses from the Ti:Sapphire lasers used in Paper I-V) and the scattering particle to be surrounded by air, then $\alpha = 1$ corresponds to a particle with a diameter of 0.13 μm. If, on the other hand, the incident light comes from a soft X-ray source with a wavelength of 1 nm, to obtain $\alpha = 1$ the scattering particle should have a diameter of 0.15 nm.

Scattering in the Rayleigh and Mie regimes is often discussed with reference to the scattering plane. As shown in Fig. 2.1, it is defined as the plane spanned by the propagation vector of the incident light and the scattering direction. The scattering is characterized by the scattering phase function and the total scattering cross-section (σ_{S}). The phase function gives the angular distribution of scattered light intensity within the scattering plane, and the total scattering cross-section gives the strength of the scattering.

Rayleigh scattering is characterized by a comparatively uniform scattering phase function with respect to changes in the size parameter. The scattering efficiency ($Q_{\mathrm{S}} = \sigma_{\mathrm{S}}/\pi d^2$), on the other hand, scales as α^4. Example of a Rayleigh scattering phase function is shown in Fig. 2.2. Here a particle with a diameter of 0.001 μm is surrounded by air and illuminated with 800 nm light ($\alpha = 8 \times 10^{-3}$). The figure shows the incident light being polarized both parallel and perpendicular to the scattering plane.

Mie scattering is characterized by a non-uniform scattering phase function with respect to the size parameter. Here an increasing α gives rise to a more dominant frontal lobe, accompanied by the development of several side lobes. The variation of the scattering efficiency is less straight forward than in the Rayleigh regime. It is characterized by an oscillatory dependence on α, su-

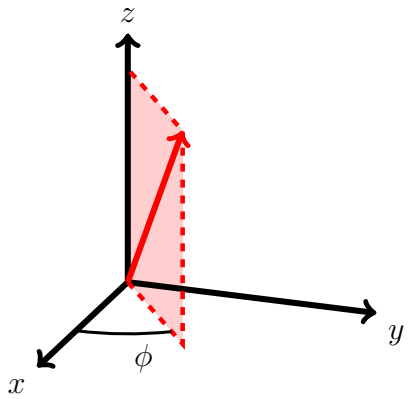

Figure 2.1: *Definition of the scattering plane (shown in light red). The scattering plane is spanned by the propagation vector of the incident light (here assumed to coincide with the z-axis) and the scattering direction (the red vector in the figure). In this geometry, the scattering plane is fully defined by the azimuthal angle ϕ.*

perimposed with a higher frequency ripple structure (see *e.g.* [16]). Scattering phase functions for fuel drops in air, with diameters of 1 μm and 10 μm, are shown in Fig. 2.3. With 800 nm light, this gives α values of 8 and 80 respectively. The figure shows incident light being polarized both parallel and perpendicular to the scattering plane. Here the increasing dominance of the forward lobe when increasing the drop diameter can be seen. This dependence on α in the Mie regime is, in fact, used by some devices, *e.g.* the Malvern particle sizer, to measure droplet sizes [17].

The polarization of light is also affected by scattering in both Rayleigh and Mie regimes. If the incident light is fully polarized, either parallel or perpendicular to the scattering plane, the scattered light maintains this polarization. If, on the other hand, the incident light is polarized with an oblique angle to the scattering plane, the scattered light will exhibit a change in its polarization. The details of the polarization change will depend on the scattering direction as well as the characteristics of the scattering object. This implies that light scattered

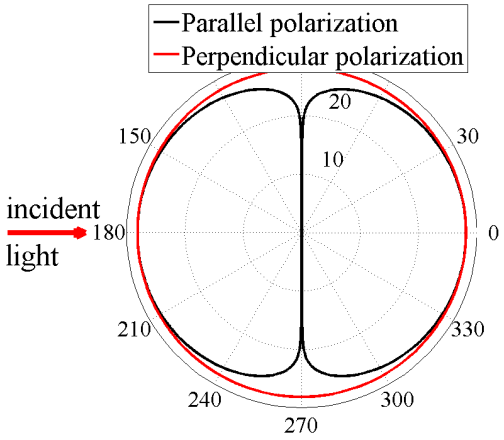

Figure 2.2: *Logarithmic plot of 800 nm light scattered from a 0.001 μm particle in air. The refractive index of the particle was 1.52, the same as for the fuel drops in Fig. 2.3. The results of incident light polarized both parallel and perpendicular to the scattering plane are shown. The phase functions are normalized to show the relative angular scattering behavior. This case corresponds to scattering in the Rayleigh regime.*

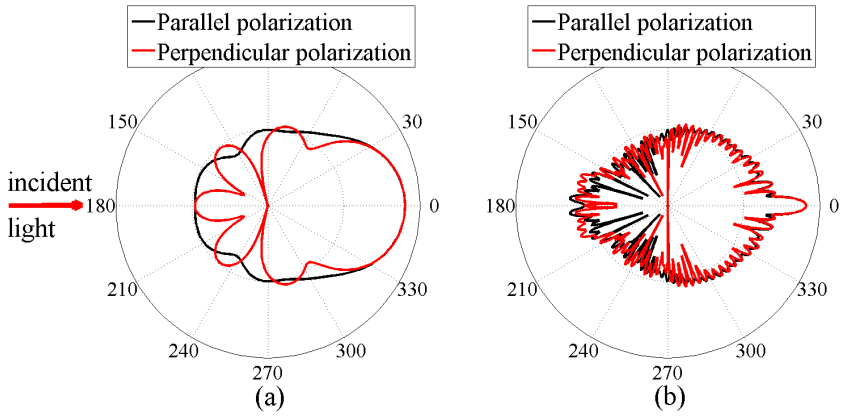

Figure 2.3: *Logarithmic plots of 800 nm light scattered from 1 μm and 10 μm fuel drops in air. Part (a) shows scattering from the 1 μm drop, and part (b) shows scattering from the 10 μm drop. The refractive index of the fuel was 1.52. The results of incident light polarized both parallel and perpendicular to the scattering plane are shown. The phase functions are normalized to show the relative angular scattering behavior. These cases correspond to scattering in the Mie regime.*

strictly in the forward direction, relative the incident light, maintains the polarization of the incident light, while light scattered off-axis generally exhibits a polarization change.

A discussion of changes in the coherence of light due to scattering requires consideration of light incident on an ensemble of drops. If the ensemble has a sufficiently low number density, contribution to the scattered light intensity due to multiple scattering can be discarded. The scattered light is said to be in the single scattering regime. If the ensemble is monodisperse, the scattered wave fronts will be identical except for their origin. This implies that on-axis scattering will be coherent. Light scattered off-axis, on the other hand, will have random phase shifts due to the position of the distributed drops. Consequently, off-axis scattering will have degraded coherence. In the case of an ensemble of drops with a distribution of sizes, both on- and off-axis scattering will degrade coherence, albeit on-axis scattering to a lesser degree.

2.2.2 Multiple scattering

The discussion in section 2.2.1 was limited to events in the single scattering regime. However, in an optically dense environment with a distribution of drop sizes, such as a Diesel spray, the light interaction is often highly affected by multiple scattering. That is, the scattered light from an initial drop interaction is subsequently scattered by a number of other drops. A detailed treatment of these scattering events soon becomes immensely complex, and requires statistical approaches like Monte Carlo simulations [18–20]. Some general insights can, however, be drawn from the discussion of single scattering in section 2.2.1:

- Multiple scattering strictly in the forward direction will maintain the initial polarization.
- Multiple scattering off-axis will cause depolarization.
- Multiple scattering, both on- and off-axis, will degrade coherence.

In the case of Diesel sprays, drop-size measurements indicate that the drops are found in the size range of 5 μm-15 μm [21–23]. In the case of optical wavelengths, this places scattering from the drops surrounding the spray formation region in the Mie regime. Since the work constituting this thesis concerns optical wavelengths, the remaining part of this section will be concerned with the Mie scattering encountered when probing these sprays.

In discussions regarding spray diagnostics with optical wavelengths, the term optical depth (OD) is often used. The term comes from the Beer-Lambert law, and is in the context of optics often written:

$$\begin{aligned} \frac{I}{I_0} &= \exp\left[-\mathrm{OD}\right], \\ \mathrm{OD} &= N\sigma_{\mathrm{ext}}L, \\ \sigma_{\mathrm{ext}} &= \sigma_{\mathrm{abs}} + \sigma_{\mathrm{s}}. \end{aligned} \tag{2.2}$$

In Eq. 2.2, I_0 is the initial irradiance (unit of W/m^2) of *e.g.* a laser beam, I the final irradiance after propagating a distance L in the medium, and N the number density of the scattering particles. The total extinction cross-section, σ_{ext}, is the sum of the total absorption and scattering cross-sections. Thus, in the absence of absorption, $N\sigma_{\mathrm{ext}}$ is representative of the average number of scattering events per unit length. OD represents the total number of scattering events occurring when propagating a distance L in the medium.

To measure the OD experimentally with light extinction measurements in situations where scattering dominates σ_{ext} is, however, ambiguous. The result will depend on both the collection angle and the size parameter of the scattering interaction. It will depend on the collection angle since this angle will determine how much of the light scattered off-axis will be included, and the size parameter since, as shown in Fig. 2.3, this parameter determines the probability for forward scattering. As an example, in a dense medium with comparatively large scattering particles, a light extinction measurement will underestimate the OD according to Eq. 2.2 because a large portion of the light is scattered multiple times in the forward direction. A measurement of the OD in an unknown scat-

tering environment cannot easily be compared to scattering from other unknown environments and/or measurements performed using instruments with different collection angles. However, as shown in Monte Carlo simulations by Berrocal *et al.* [24, 25], for cases with comparably large particles, where scattering is dominated by the forward lobe, the average number of scattering events contributing most to the light signal is roughly equal to the OD. Therefore, in these cases, OD is still a useful conceptual tool when discussing scattering effects on the light signals acquired with optical measurement techniques.

The work presented by Berrocal *et al.* [24, 25], and later discussed by Linne [8], uses a Monte Carlo code to simulate light propagation through scattering media. In the simulation, an 800 nm Gaussian light pulse with a $\sim$100 fs pulse length (full width at half maximum (FWHM)) was propagated through a 10 mm path length cuvette, filled with a suspension of distilled water and polystyrene (PS) spheres. The number density of the spheres was varied in accordance with Eq. 2.2 to give rise to ODs ranging from 5 to 15. The light pulse was modeled as a collection of energy parcels, propagating along straight trajectories until a scattering event occurred. The length between scattering events was given by the mean free path associated with the Beer-Lambert equation. In a scattering event, the light parcel changed trajectory based on a probability distribution analogous to the scattering phase function (*e.g.* Fig. 2.3). The transmitted light could be analyzed based on its off-axis angle, temporal characteristics, and accumulated number of scattering interactions before reaching the detector (scattering order). The simulation was performed for both 1 μm and 5 μm sphere sizes, corresponding to size parameters of 7.9 and 39.3. The study by Berrocal *et al.* shows that up to an OD of 5 (calculated with Eq. 2.2), the light signal propagated through the scattering medium still consisted of a large portion of un-scattered light (also called ballistic light). At ODs higher than 5, the ballistic part of the signal decreased rapidly and became very small. Instead, the bulk of the transmitted signal consisted of scattered light of various scattering orders. The characteristics of the signal depended on the scattering size parameter. For the smaller sphere size, characterized by a broader forward

scattering lobe, the light pulse was dominated by light multiply scattered off-axis. The off-axis scattering stretched the pulse in time. For the larger sphere size, on the other hand, the signal was dominated by light scattered multiple times on-axis. This light exited the scattering medium shortly after the ballistic light and, consequently, the signal was temporally broadened to a lesser degree than in the small particle case.

When it comes to interpreting the results by Berrocal *et al.* in the context of imaging through scattering media, several notes can be made. Ideally, one wants the signal to be made up by ballistic, un-scattered light, as much as possible. This is the case since this light is unaffected by the scattering, thereby retaining the potential image information from within the medium. This case holds for ODs up to 5 for both simulated sphere sizes. Consequently, schemes like ballistic imaging for transillumination are not necessary to provide liquid/gas interface images in this case.

When the OD is increased above 5 (roughly), multiply scattered light will start to dominate the light signal. Here one will start to see differences depending on the size of the scatterers. In the small sphere size limit, the broader forward scattering lobe will result in more of the light being multiply scattered off-axis. Such light is corrupted when trying to recover information from the interior. Image information acquired within the medium is effectively washed out by the scattering. To recover the image signal, some kind of filtering must be employed. At the highest simulated optical depth, OD=15, however, the signal is completely dominated by the off-axis scattering. Here, arguably no information could be recovered regardless of the filtering scheme.

For larger scattering particles, the situation is somewhat different. As before, the signal is dominated by multiply scattered light, but due to the scattering phase function, multiple scattering will predominantly take place in the forward direction. The signal will not be as spread out, neither temporally nor spatially. This trend will be more pronounced with increasing particle size. Light scattered in the forward direction will not be as corrupted as light being scattered

off-axis. For a given number of scattering events, less image information acquired inside the medium will be lost in the case of larger particles as compared to smaller ones. It must, however, be pointed out that with increasing OD, image information will be lost here as well, both because of the probability of off-axis scattering and the finite width of the forward scattering lobe. Filtering will help recover the signal, but since the signal spread is shorter both in time and space, it can be more difficult than for smaller spheres.

2.3 Diagnostics in the spray formation region

The challenges involved in performing experimental investigations in the spray formation region of atomizing sprays have spurred development of specialized non-intrusive diagnostic techniques. These techniques can be categorized based on electromagnetic radiation with optical wavelengths (including soft ultraviolet (UV) and IR) and electromagnetic radiation in the X-ray regime (including hard UV). For optical wavelengths where multiple scattering from drops can be a major impediment to reliable measurements, the techniques employ dedicated schemes to reduce the unwanted noise. When using X-rays, on the other hand, the difference in refractive index between air and liquid fuels is sufficiently small for scattering from the droplet cloud to only affect the measurements weakly. Current development of diagnostic techniques for the spray formation region have recently been reviewed elsewhere [8, 26, 27]. Therefore, the intention of this section is not to give a detailed overview of current research directions. Instead, a few techniques will be discussed to place the current work in context, and to highlight the different types of obtainable data.

Structured illumination is a technique used for planar laser imaging, and as such, it can be used in efforts to measure *e.g.* droplet size distributions and species concentrations. It has been assessed to be functional up to an OD of 6, which places its operating region below the most dense spray conditions [8]. X-ray radiography can give quantitative line-of-sight liquid mass distributions

regardless of OD, but currently the data is averaged over many injection events at single points in the spray. The aim of the techniques investigated and developed in this thesis, on the other hand, is to provide single-shot images of liquid structures in dense scattering environments. As discussed in Chapter 3 and 4, ballistic imaging generates line-of-sight images of larger liquid structures in dense scattering conditions, and time-gated sectioning aims to obtain depth-resolved backscatter images, which can potentially yield structural information about the core of the jet. Thus, these various techniques provide different types of information and can complement each other to give a more detailed understanding of the sprays of interest.

2.3.1 Structured illumination

Structured laser illumination planar imaging (SLIPI) is a technique to filter multiple scattering noise by image post-processing. It was originally developed for microscopy-related research (see *e.g.* Neil and Breuninger [28, 29]), and was adapted to a spray and combustion context by Kristensson *et al.* who investigated the Mie scattering from a hollow cone water spray [30, 31]. In spray-related research it has most often been employed together with two-dimensional laser based planar imaging techniques. In planar laser imaging, the laser beam is formed into a laser sheet that illuminates the object. The signal is subsequently recorded in a side-scattering arrangement. Various methods are based on this geometry, and can therefore benefit from the noise reduction by SLIPI. The technique is based on imposing a spatial intensity modulation in the incident laser sheet. This can be done by placing *e.g.* a Ronchi grating in the beam path. Singly scattered light will maintain this spatial modulation. Light scattered multiple times off-axis, on the other hand, will lose the intensity pattern. By capturing a number of images (subimages) with certain relationships between the phases of their intensity modulation, a non-modulated image containing singly scattered light can be reconstructed. In [32] Kristensson *et al.* assess the SLIPI technique to be functional in turbid environments up to an OD

of $\sim$6.

In 2012, Berrocal *et al.* applied the technique to a Diesel spray injected with 1100 bar into room temperature at 18.6 bar [33]. The authors evaluated how multiple scattering suppression by SLIPI could improve the results of planar droplet sizing (PDS) when measuring drop size distributions. PDS uses the ratio of the intensity profiles from two images to calculate the drop size distribution [34]. The liquid, doped with a fluorescent dye, is illuminated with a laser plane. Images of both the elastic scattering (Mie) and the fluorescent signal are recorded. Berrocal *et al.* showed that multiple scattering has a significant adverse effect on the PDS image, and suppressing it with SLIPI is indeed possible. More recently Mishra *et al.*, investigated the SLIPI-PDS setup in more detail [35]. Data for both more conventional PDS and SLIPI-PDS were calibrated and compared with a phase doppler anemometry (PDA) system to measure the absolute droplet size distribution in a spray from a pressure swirl nozzle. The authors concluded that when using SLIPI-PDS, as opposed to more conventional PDS setups, it was possible to get quantitative size distributions by calibration with PDA. The more conventional PDS setup failed to achieve this due to multiple scattering errors. In 2012, Chartier *et al.* investigated wall-jet air-entrainment in an optically accessible Diesel engine in a non-combusting case [36]. With the SLIPI technique, scattering from the combustion chamber walls could be suppressed and local equivalence ratios near the piston bowl could be measured.

One complicating factor with the SLIPI technique is that a number of consecutive images must be captured in order to reconstruct the image. Unless time averaged data are sought, this places limitations on the velocity of the flow field to avoid motion blur. Efforts to overcome this problem have been made. Kristensson *et al.* introduced what was called nanosecond-SLIPI where the output from three Nd:YAG lasers were used [37]. To get the intensity modulation, a grating was placed in the beam path of each of the beams. The three images were recorded with a high-speed multiframe camera. With this setup, the image triplet could be captured in less than 40 ns. Another route of experimentation to

improve temporal resolution has been to reduce the number of subimages used to reconstruct the SLIPI-image. Kristensson *et al.* proposed a setup using only two images [38]. However, using only two subimages in the reconstruction will cause modulation artifacts to be present in the SLIPI-image. If the effects of the residuals can be suppressed to generate acceptable errors in the signal, the approach will be an important step in order to get higher temporal resolution from setups less complex than the nanosecond-SLIPI.

2.3.2 X-ray radiography

A number of aspects are different when using X-rays compared to using optical wavelengths. Constructing optical components is much more complicated with X-rays than with visible wavelengths. Moreover, the refractive indices encountered in most material are typically very close to, and slightly less than one. Consequently, X-rays scatter and reflect very weakly. The light is refracted due to differences in the refractive index when passing through droplets and larger fluid structures, but stays within the beam profile. Instead, the dominant interaction with matter is absorption. X-ray radiography is an absorption-based technique, utilizing absorption differences between different media and phases. An X-ray beam, or pulse, illuminates the object, and the attenuation of the beam is measured with a detector in a line-of-sight configuration. The attenuation of the X-ray intensity will scale in accordance with the Beer-Lambert law in the absence of scattering (Eq. 2.2). If an X-ray source with narrow enough bandwidth is used, the attenuation can be used to obtain quantitative data of the line-of-sight projected mass (kg/m^2). Using a broader bandwidth, effects of wavelength-dependent differences in absorption coefficients complicate this procedure. Typically, the X-ray beam is focused at a point in the spray, and the attenuation is measured there. The spray is subsequently raster-scanned to reconstruct a 2D attenuation map. The resolution of the measurement depends on the steadiness of the spray, the size of the focal point, and the step size of the translator stages moving the spray. As an example, Duke *et al.* reported using

FWHM spot sizes around 30 μm^2 with a raster-scan spacing of 35 µm-75 µm, when performing a radiography based tomographic measurement of the spray from a gasoline injector [39]. Focusing the beam and raster-scanning the spray is, however, not the only option. In 2014, Halls *et al.* reported on a comparison between raster-scanned data, and radiography data from a wider beam imaging setup using an X-ray tube source [40]. Unfortunately, X-ray radiography provides rather low signal to noise ratios for materials made of lighter atomic elements such as organic materials like liquid fuels. The reason is that the absorption cross-section decreases with decreasing atomic number [41]. To overcome this and obtain reliable data, each scan position is sample averaged over an ensemble of measurements. Consequently, even though each measurement can be time resolved, the two dimensional map of the liquid mass distribution is a statistical average over many injection events. For recent publications using the technique, see *e.g.* Radke *et al.*, Duke *et al.*, and Pickett *et al.* [39, 42, 43]. In [42], Radke *et al.* reported on simultaneous gas- and liquid phase distributions using a combination of X-ray radiography and X-ray fluorescence. In [39], Duke *et al.* investigated the spray from a gasoline direct injection injector with radiography based tomographic reconstruction. Pickett *et al.* used radiography to study the Engine Combustion Network (ECN) spray A in [43].

Chapter 3

Ballistic imaging

3.1 Introduction

BI is a technique designed to obtain images of larger refractive structures from within scattering media. Like SLIPI, it originated in the medical community [44]. In 2004, Paciaroni *et al.* adapted the technique and used it in the context of spray research, investigating a turbulent water jet [45]. The term ballistic comes from the concept of ballistic light as discussed in Chapter 2.2. In a general sense BI is a shadow-imaging arrangement where schemes to suppress the contribution of corrupted light have been employed. It is designed to generate single-shot line-of-sight images of liquid/gas interfaces of larger liquid structures in the spray formation region. BI has been applied to a variety of sprays, *e.g.* to a water jet in cross-flow [46], to an effervescent spray [47], to a rocket injector spray [48], and to heavy-duty Diesel sprays under various conditions [49–51].

A promising development of the BI technique is what can be called velocity-BI. Here a sequence of images are captured using BI, and subsequently pro-

cessed using image correlation velocimetry (ICV) techniques. From the correlations, time-dependent properties such as velocities of the liquid structures in the spray formation region can be deduced. They can thus provide detailed information regarding the dynamics of the breakup. In 2006, a two-pulse velocity-BI system capable of capturing two-dimensional velocity was successfully demonstrated in a proof-of-concept sense on a liquid jet in the dripping regime [52]. It was applied to such a slow moving object since the system was limited to pulses from a single regenerative laser amplifier emitting pulses with a 1 kHz repetition rate. Thus, the time between correlation images was 1 ms. The system was subsequently improved with the use of two synchronized laser amplifiers allowing much shorter time separation of the images, and applied to a more challenging aerated spray [53]. In Paper II of this thesis, the two-pulse system used by Sedarsky *et al.* in [53] was further improved with a third laser amplifier. Now a sequence of three images can be captured. In this way, two velocity correlations can be calculated, and by differencing them, accelerations can be inferred.

As discussed in section 2.2, useful imaging light is ballistic light and light scattered strictly in the forward direction. Corrupted light is light scattered multiple times off-axis. When light that initially carries image information regarding larger structures inside the spray scatters off-axis from the drops, the image information will be degraded and lost. If this light is allowed to contribute to the image, it can prevent non-corrupted image information from being discernible. The scattering will result in changes in direction of propagation, changes in the polarization state, and a reduction of coherence. These changes take place with probabilities depending on the wavelength of the light, the size of the scattering particles, and differences in refractive indices. The combination of off-axis scattering together with several scattering events results in multiply scattered light leaving the spray within a larger solid angle, at a later time than ballistic light, causing both a spatial and temporal spread of the light pulse. Thus, the characteristics that can be used to mitigate the amount of corrupt light reaching the camera are the spatial confinement of the light leaving the spray, its

polarization, its time dependence, and its lack of coherence.

3.2 Spatial, polarization, and coherence gating

Examples of ways to gate, or filter, the image signal based on its spatial and polarization characteristics are shown in Fig. 3.1. Figure 3.1(a) shows how

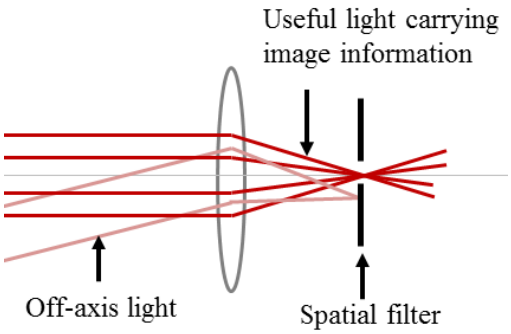

(a) Spatial gating

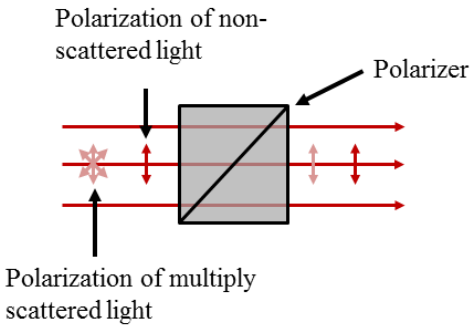

(b) Polarization gating

Figure 3.1: *Schemes to reject multiply scattered off-axis light using spatial and polarization filtering. Multiply scattered off-axis light is shown in a different color to ease interpretation of the figure.*

spatial gating can be accomplished by using one or more lenses when relaying the image to the camera. An aperture is placed in a focal, or Fourier, plane of a lens. The size of this aperture will decide how much of the off-axis light will be transmitted further down in the optical train. There will be a trade-off between off-axis light rejection and blocking of higher spatial frequencies in the image. It should be noted that by just having optical components in the path between the object and the detector some off-axis light will be rejected, *i.e.* the finite aperture of the components act as a soft spatial filter. Figure 3.1(b) shows a way to perform polarization gating. It can be done by maintaining the incident light in a well-defined polarization state, and placing a polarizer with its transmission axis parallel to the polarization of the incident light in the optical path after the spray. Light being multiply scattered off-axis inside the spray will leave it with degraded polarization. Hence, the corrupted light will be suppressed.

Coherence gating uses the fact that coherence is lost during the multiple scattering process. One way of arranging this gating is through second harmonic generation (SHG) by crossing the imaging beam and a reference beam (or gating beam) in a SHG crystal after the turbid medium [50, 54, 55]. Since coherence is a prerequisite for SHG, the generated frequency doubled light can carry image information from the ballistic components of the image light pulse. Idlahcen *et al.* applied SHG-based coherence gating to a spray in [50]. The setup was applied to a Diesel spray injected through a 200 μm nozzle into atmospheric conditions with a pressure of 400 bar. The light source was a Ti:Sapphire laser generating 800 nm light pulses with pulse lengths $\sim$100 fs, and β-Barium Borate (BBO) was used to generate the SHG signal in a crossed beam geometry. This experimental setup resulted in reported gate times of 270 fs, and a spatial resolution of 10 μm without scatterers present. It should be noted here that with the use of short-pulse lasers the coherence gating technique is effectively acting as a time-gate. However, this particular time-gate relies on the existence of coherent light after the spray. As argued by Linne in [8], in very dense sprays it is likely that there is not enough coherent light for it to be possible to use coherence gating to reliably generate single-shot images.

3.3 Time-gating

Time-gated ballistic imaging was popularized by the Alfano group in the early 1990s [56, 57]. The technique relies on the effects described by the Monte Carlo modeling by Berrocal *et al.* [24, 25], discussed in section 2.2.2. The modeling shows that a 100 fs laser pulse that propagates through a 1 cm thick scattering medium experiences a temporal spread of several picoseconds, with most of the useful imaging light in the first picosecond of the transmitted signal. Thus, to be able to employ a time-gate, or time filter, the spray must be illuminated by a light pulse that is substantially shorter than the expected temporal spread. In addition to a very short light pulse, the device providing filtering in the time domain must be able to create a transmission window short enough to isolate the useful imaging light from the corrupted light. This is not straightforward since the time scales involved are too short for both mechanical shutters and commercially available electro-optics. Instead, what can be employed to stimulate a device operating on these short time scales is the same short pulse that is used to illuminate the spray. In that sense, time-gating is similar to the SHG-based method of coherence gating. Time-gating, however, has been implemented using the optical Kerr effect (OKE), and by relying on the Kerr effect, coherence is not a limiting factor. By carefully positioning the activation time of the OKE-gate relative the image pulse, useful imaging light can be transmitted through the gate while a significant part of the corrupted light is rejected. In very dense sprays, the OKE-gated image is dominated by light that is multiply scattered in the forward direction. This light carries image information, although degraded to a certain extent due to the spatial width of the forward lobe of the scattering phase function.

3.3.1 Optical Kerr effect

The optical Kerr effect is a change in the refractive index of certain materials when they are subjected to high optical intensities. The OKE response of these

materials can be written:

$$n(\vec{\boldsymbol{r}}) = n_0 + n_2 I_g(\vec{\boldsymbol{r}}). \tag{3.1}$$

In Eq. 3.1, I_g is the optical intensity, n_0 and n_2 the linear and non-linear refractive indices respectively, and $\vec{\boldsymbol{r}}$ represents a radial vector orthogonal to the direction of propagation of the light beam [58]. In initially isotropic media, the change in the refractive index will occur along the polarization axis of the light pulse, and it will induce an anisotropy in the refractive index, called a birefringence. This birefringence can be used as a time-gate. Using an intense laser gate pulse (I_g) to induce a time-dependent birefringence in the Kerr medium, part of a much weaker image pulse (I_i) can have its polarization rotated due to the induced birefringence. Consequently, only the part of the imaging pulse present during the transient birefringence event will experience the rotation. By using proper means to segregate light based on its polarization, this effect can be used to gate the image pulse in time.

By setting the polarization of the gate pulse at 45° relative the image pulse, the polarization of the image pulse can be decomposed into two equally large orthogonal components, where one component is parallel to the polarization direction of the gate pulse, and the other is perpendicular to it. The two components will propagate through different refractive indices, and a phase difference (ϕ) between the components will develop as they pass through the medium. The phase difference can be expressed as

$$\phi(\vec{\boldsymbol{r}}) = \frac{2\pi\ L\Delta n(\vec{\boldsymbol{r}})}{\lambda} = \frac{2\pi\ L n_2 I_g(\vec{\boldsymbol{r}})}{\lambda}. \tag{3.2}$$

In Eq. 3.2, $\Delta n = n_2 I_g$ is the difference in refractive indices experienced by the two components of the image pulse, and L is the length of the birefringent medium. Thus, the Kerr medium will act as a waveplate, rotating the polarization of the image beam. By placing a polarizer after the Kerr medium that is crossed relative the polarization of the incident image pulse, only the component of the image pulse parallel with the transmission axis of the polarizer will be transmitted. The transmitted light intensity after this crossed polarizer

is given by

$$I_i = I_{i,0} \sin^2 \left[\frac{\phi(\vec{r})}{2}\right]. \tag{3.3}$$

In Eq. 3.3, $I_{i,0}$ indicates the initial intensity of the image pulse. As can be seen in Eqs. 3.2 and 3.3, both the intensity of I_g and the interaction length will affect the induced polarization rotation and, thus, the gate efficiency. Ideally, the rotation should be 90°, which corresponds to a phase difference of half a wavelength of the image light. In reality, however, this is difficult to achieve for the whole transverse profile of the image pulse. The reason for this is the spatial intensity profile of the gating pulse, which induces a refractive index profile varying in the $\vec{r}$ direction of the gate pulse. However, even though perfect polarization rotation for the whole transverse plane of the image pulse is difficult to achieve, good overall gating efficiencies can be obtained by having a gate pulse with a beam width substantially larger than the image pulse. The spatial profile of the refractive index can also cause other aberrations in the generated images. In Paper I of this thesis it is shown that the spatial profile of the refractive index can have an effect similar to a gradient-index lens. Consequently, the Kerr medium will act as a weak cylindrical lens, and induce image aberrations.

When using these materials in a time-gating application, and thus subjecting them to optical pulses with pulse lengths ∼100 fs, the temporal behavior of the induced birefringence becomes important. Solid state materials, where the induced birefringence is mainly due to the instantaneous electronic response, often exhibit very fast rise and decay times. The total response time can be on the same order of magnitude as the length of the optical pulse. The nonlinear refractive index is, however, usually small for solid state materials suitable for imaging applications; for example Silica has a nonlinear refractive index $\sim 3 \times 10^{-20}$ $\mathrm{m^2W^{-1}}$ [59]. Thus, good gating efficiencies require very high intensities in the gating pulse. Certain liquids, on the other hand, exhibit larger nonlinear indices. Their rise and decay times are, however, considerably longer. This is due to the contribution of the slower processes of molecular redistribution and relaxation to the induced birefringence.

Carbon disulfide, CS_2, is a liquid exhibiting a large nonlinear refractive index. Ganeev *et al.* reported a nonlinear refractive index of $\sim 3\times10^{-19}$ m^2W^{-1} [60]. Due to its large n_2, it has been the Kerr medium most often used in BI of sprays. It is also the Kerr medium used in the papers constituting this thesis (Paper I-V). As an example, one can assume a 100 fs gate pulse centered on 800 nm with a radius of 4 mm ($1/e^2$), and a Gaussian pulse profile in both time and space. Using Eqs. 3.2 and 3.3, a 10 mm length of the CS_2, the n_2 value from [60], and neglecting scattering and absorption losses, it can be shown that a 100% gating efficiency on the optical axis can be achieved with a gate pulse energy of 0.35 mJ. The rise and decay process of CS_2 is complex, with several different contributing mechanisms [61, 62]. Heisler *et al.* have reported a rise time $\sim$0.14 ps and a dominant decay time of $\sim$1.7 ps [62]. Idlahcen *et al.* proposed the following expression for the temporal behavior of the induced birefringence in CS_2 using a single decay mode [63]:

$$\Delta n(\vec{r},t) \propto n_2 \int_{-\infty}^{t} I(\vec{r},\tau) \exp\left[-\frac{t-\tau}{\tau_0}\right]\left\{1-\exp\left[-\frac{t-\tau}{\tau_r}\right]\right\} d\tau. \quad (3.4)$$

In Eq. 3.4, t denotes the time, and τ_r and τ_0 are the rise and relaxation times of CS_2 respectively. The results of a simplified version of this model, where the refractive index change is only calculated along the optical axis, is shown in Fig. 3.2. Here the pulse length of the gate pulse was 100 fs (FWHM), and the τ_r and τ_0 values were 0.14 ps and 1.7 ps respectively.

In spray-related work, the OKE time-gate has been employed in two different geometries; the crossed-beam and the collinear gating geometries, which have different gating characteristics.

3.3.2 Crossed-beam gating

A crossed-beam gating geometry is shown in Fig. 3.3. This was the OKE-gate used by the group at the City University of New York [44], and later by Paciaroni *et al.* [45] when adapting the BI technique to spray investigations.

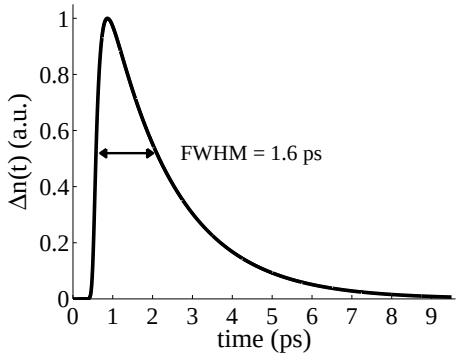

Figure 3.2: *Normalized temporal response of Δn calculated on the optical axis of the gate pulse using the model by Idlahcen [63]. A Gaussian pulse profile was assumed in both time and space. The pulse length was 100 fs, and the τ_r and τ_0 values were 0.14 ps and 1.7 ps respectively.*

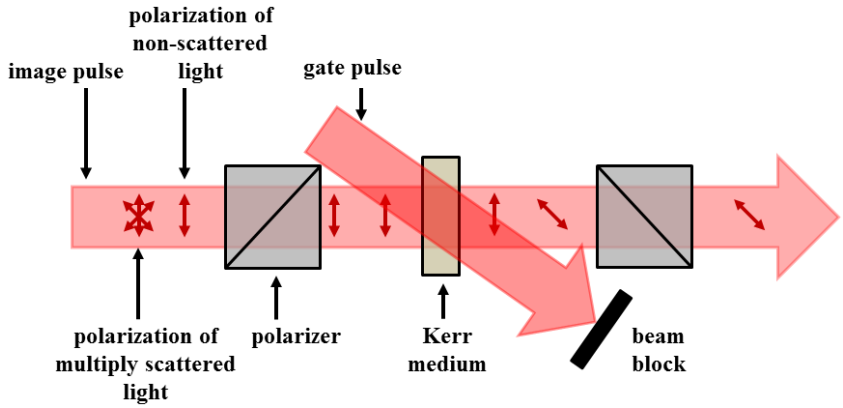

Figure 3.3: *Crossed-beam OKE-gating. Both image and gate pulses have the same wavelength.*

The Kerr medium is situated between two crossed polarizers. The first OKE-gate polarizer is positioned with transmission axis parallel to the polarization of the image pulse, and acts as a polarization gate. It furthermore ensures a well-defined polarization of the image pulse before transmission into the Kerr medium. The second OKE-gate polarizer is crossed with respect to the first, and rejects image light not exhibiting polarization rotation. The crossed-beam geometry has most often been employed using image and gate pulses at the same wavelength. Consequently, the gate pulse must propagate across the Kerr medium with a sufficiently steep angle to avoid having significant gate beam light scattered into the last OKE polarizer and on to the camera.

Since the two pulses are centered on the same wavelength, they will propagate with the same velocity through the Kerr medium. They will, however, propagate along different paths, and as a consequence there will be a temporal delay between the pulses as they propagate through the Kerr medium. As reported by Purwar *et al.* [64], this delay will cause a temporal dependence on the gating efficiency that varies across the width of the image pulse; *i.e.* a spatio-temporal coupling in the transmitted image light. The coupling will depend on the length of the Kerr medium, the width of the image beam, and the angle between the pulses. Using the refractive index data and the Cauchy parameters for CS_2 reported by Samoc [65], the effective refractive indices affecting the propagating velocity can be calculated. Assuming pulses centered on 800 nm and an angle of 11° between the gate and image pulse, a time delay of 0.1 ps/mm between the image and gate pulses will be introduced. For gate lengths of a few picoseconds, the effects of this spatio-temporal coupling are typically small, but can become significant with shorter gate lengths, steeper crossing angles, and larger image pulse widths. In previous work using a crossed-beam gating geometry with CS_2 as the Kerr medium, a path length of 10 mm CS_2 has often been used. This arrangement has provided a sufficient interaction length for available gate pulse energies to generate good efficiencies. In Fig. 3.4, an experimentally measured crossed-beam OKE-gate function is shown. In this experimental setup, CS_2 was used as the Kerr medium, with a path length of

10 mm and an 11° angle between the image and gate pulses inside the CS_2. The gate length around 1.5 ps was measured using a non-scattered image pulse as the probe.

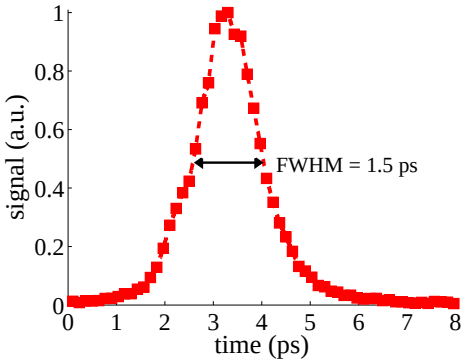

Figure 3.4: *Experimentally measured transmission of a crossed-beam OKE-gate. A 10 mm CS_2 cell was used as the Kerr medium, and the angle between the image and gate pulses inside the CS_2 was 11°.*

In the past, the crossed-beam OKE-gate has been positioned in both intermediate image and Fourier planes. Locating the gate in these different planes has different effects on the generated image. If the OKE-gate is positioned in a Fourier plane it will affect the spatial resolution of the image; the gate will act as a low-pass filter. Positioning of the OKE-gate in an image plane, on the other hand, reduces this spatial filtering effect, but places constraints on the size of the intermediate image. Furthermore, Idlahcen *et al.* have shown that locating the single-color crossed-beam OKE-gate in an image plane generates high levels of gate pulse scattering in the images [63]; gating in a Fourier plane reduces this scattering. Consequently, Idlahcen *et al.* argued that Fourier plane gating is the preferred option for the single-color crossed-beam geometry.

3.3.3 Collinear gating

An alternative to using the crossed-beam geometry is to have the image and gate pulses propagate collinearly. However, since the pulses then propagate along the same path, new measures must be taken to prevent excessive gate light from reaching the camera. One way to do this is to use different wavelengths for the image and gate pulses. The gate pulse can then be removed from the optical path using a suitable bandpass filter. In a spray context, this OKE-gate geometry was first reported by Purwar *et al.* [64]. The authors reported improved spatial resolution as compared to a crossed-beam geometry; an ultimate resolution of 96 line-pair/mm (lp/mm) for the collinear setup as compared to an ultimate resolution of 38 lp/mm for their crossed-beam setup. This improvement was attributed to both the removal of the spatio-temporal coupling, and the possibility to locate the OKE-gate in an image plane. Due to the suppression of the gate pulse using a bandpass filter in the collinear geometry, the OKE-gate can be positioned in an image plane without excessive gate pulse scattering in the generated images.

An example of a collinear OKE-gate geometry is shown in Fig. 3.5. Here the gate beam is routed into the optical path of the image beam using a dichroic mirror (a component acting as a good reflector for a certain wavelength region while being transparent for other regions). After the Kerr cell, the gate beam is blocked using a suitable bandpass filter, preventing it from reaching the detector.

To create pulses with different wavelengths, one can frequency double a part of the original laser output with SHG using a nonlinear crystal. If the laser pulses come from a Ti:Sapphire based system, this means having one pulse centered on 800 nm and the other on 400 nm. However, when using pulses with different wavelength spectra, dispersion can cause them to propagate with different velocities. This velocity difference will introduce a time delay between the image and gate pulses, which will depend on the propagation length in the dispersive medium. Using the data from Samoc [65], the effective refractive

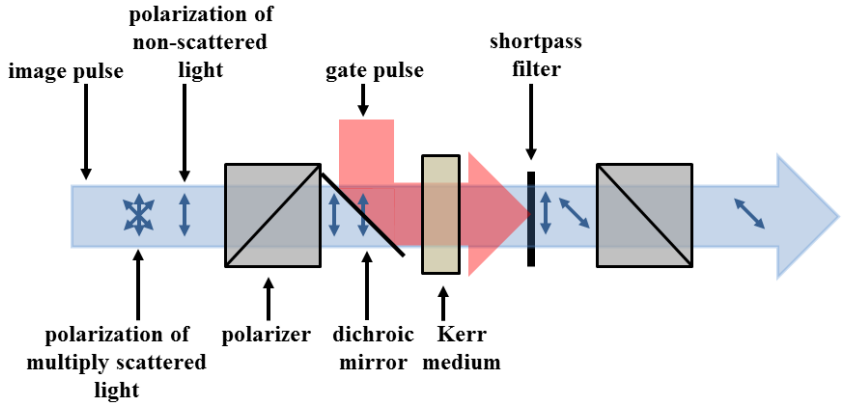

Figure 3.5: *Collinear beam OKE-gating. Image and gate pulses have different wavelengths.*

indices (group indices) at 800 nm and 400 nm can be calculated to $n_{800\text{nm}} \approx 1.6$ and $n_{400\text{nm}} \approx 2.0$. Using these refractive indices, the induced time delay due to the velocity difference will be around 1.2 ps/mm. Thus, the path length of the Kerr medium must be short as compared to the case of a single-color OKE-gate, in order to provide short time-gates. Purwar *et al.* investigated path length effects using 10 mm, 2 mm, and 1 mm path length CS_2 cells, respectively [64]. Their experiments showed a strong dependence of the CS_2 path length on the gate length. The 10 mm path length cell had a gate length of around 11 ps, and the 1 mm cell had a length of around 1 ps, both measured as FWHM.

3.4 Imaging configurations

Examples of two OKE-gated optical setups are shown in Fig. 3.6. The main difference between the two setups is in the method of relaying the image to the camera. The setup in Fig. 3.6(a), here called the 4*f* setup, is similar to the arrangement used in earlier work by the Alfano group [56, 57]. The setup was

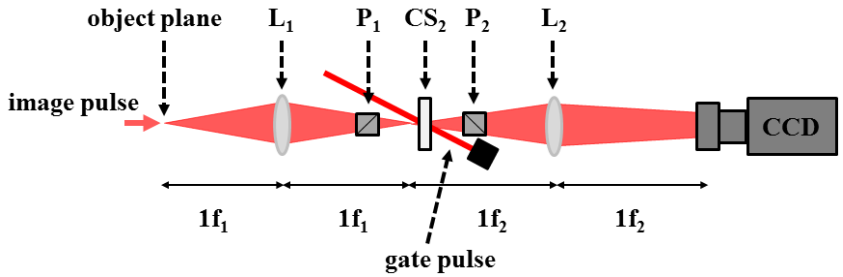

(a) 4*f*-setup

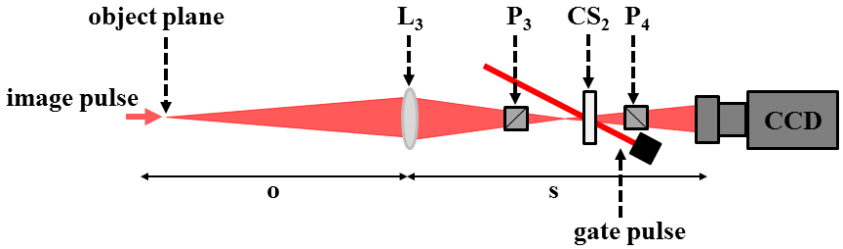

(b) 2*f*-setup

Figure 3.6: *Imaging configurations used in BI. Part (a) shows the 4f-setup, and part (b) shows the 2f-setup.*

subsequently inherited when the BI technique was adapted and used in early BI spray studies [45]. The setup in Fig. 3.6(b), here called the 2*f* setup, was first described by Schmidt *et al.* [48]. It is less complex than the 4*f* setup, and generated what appeared to be similar image quality as compared to the 4*f* setup. The double lens setup is referred to as 4*f* since it is principle a standard 4*f* correlator used in Fourier optics. The single lens setup, on the other hand, is referred to as 2*f* since it is a more classical imaging setup and resembles the one-to-one magnification achieved when placing the collecting lens 2*f* behind the object. The results from Schmidt *et al.* indicated that for time-gated ballistic imaging in atomizing sprays, the Fourier-imaging style used in the 4*f* is not the only option; simpler setups can be used for spray studies. In 2011, Sedarsky *et al.* published a detailed model comparing the 2*f* imaging setup to a 4*f* projection setup [66]. Here, the 4*f* setup was modeled as a non-focused setup as opposed to the experimentally focused setup. In the work of Sedarsky *et al.*, the output of a Monte Carlo code that modeled the light scattering in the turbid media was coupled with a commercial ray-tracing code used to model the optical system. The modeling by Sedarsky *et al.*, which produced very good agreement with the experimental contrast transfer functions (CTF) by Paciaroni [45], demonstrated that the size of the scattering particles (*i.e.* their scattering phase function) determines the regimes in which each optical setup performs best. In their comparison, contrast from a single spatial frequency (1 lp/mm) was investigated and the 2*f* setup generated higher contrast than the non-focused 4*f* in the large-particle limit (15 μm PS spheres in water). In the small-particle limit (0.7 μm PS spheres in water), on the other hand, the 2*f* setup generated lower contrast. Sedarsky *et al.* argued that the reason for these results lies in the scattering phase function of the spheres. The 2*f* setup with its longer object-to-lens distance performs better in situations dominated by forward scattering than in the more diffuse scattering generated by small particles. The non-focused 4*f* projection setup, on the other hand, preferentially transmits forward scattered light while suppressing diffusively scattered light, and performs better in the small-particle limit. However, the resultant CTFs of the two modeled setups have not previously been investigated experimentally; neither has a comparison

between a focused $4f$ setup and the $2f$ setup been made. Such a comparison is performed in Paper I of this thesis. Here the $2f$ setup and the focused $4f$ setup are investigated using both experimental and computational techniques.

Chapter 4

Time-gated sectioning

As shown in *e.g.* images published in Paper III and Paper IV of this thesis, BI generates line-of-sight images of larger refractive structures inside the spray formation region. The images in Paper III and Paper IV indicate a liquid core that grows radially in the downstream direction. This could for example, indicate a core consisting of overlapping liquid sheets, separated by entrained air. The hypothesis of overlapping liquid structures finds some support by X-ray radiography measurements under milder conditions, which have shown that the fuel volume fraction in the core is often less than 100% [67]. To draw further conclusions using BI is, however, difficult. Since BI generates path-integrated images, large overlapping refractive structures cannot be accurately resolved. Therefore, a technique capable of generating depth-resolved information, *i.e.* a form of optical sectioning, of the spray formation region could provide additional information regarding the breakup processes. It could for example, shed further light on the question regarding the apparent downstream growth of the liquid core.

One way to obtain depth-resolved images from highly atomizing sprays is to use other methods than line-of-sight integrated imaging. SLIPI (discussed

in section 2.3.1) is a laser sheet imaging technique that has successfully been applied to detect singly side scattered light in moderately dense sprays. Since the side scattered light from the thin laser sheet is detected, the images will be depth-resolved. SLIPI has, however, been assessed to be functional up to an OD $\sim$6 [32]. The technique can thus run into difficulties when probing the spray formation region of highly atomizing sprays.

The use of backscattered light in depth-resolved imaging has mainly been limited to techniques designed for fields other than spray research. Examples of such techniques are optical coherence tomography (OCT) and spectral polarization difference imaging (SPDI), both stemming from the medical imaging community [68–70]. In OCT, singly backscattered light from a white light beam initially focused inside tissue, is detected using interference from a reference beam. Multiply scattered light will have progressively degraded coherence, and will therefore not contribute to the interference. In OCT, the image is formed by raster scanning the sample either in a transverse plane and/or in depth. In SPDI and related techniques, polarization characteristics of the backscattered light are used to suppress unwanted contributions to the image. Incident light with a well-defined polarization state illuminates the sample and the backscattered image is filtered with additional polarizers. Backscattering from the sample surface will predominantly maintain the polarization state of the illumination light, while multiple light scattering from within the sample will have lost its initial polarization. In this way, contributions from surface and sub-surface scattering can be differentiated. Generating and combining images using different illumination wavelengths, the wavelength-dependent penetration-depth can be used to accentuate depth within the sample. OCT, SPDI, and related backscattering techniques are, however, probably not applicable to investigations in the spray formation region. In the case of OCT, there are an insufficient number of coherent photons to construct an image within the time frame required to avoid motion blur [8]. In the case of SPDI, the depth-resolution will likely not be sufficiently high to probe the liquid core in the spray formation region of modern DICI engine fuel sprays.

A different approach to depth-resolved backscatter imaging is to sample the light with a time-gate. Here the depth-resolution would come from differentiating light based on its time-of-flight (*i.e.* its traversed optical path length (OPL)). In 2005, Zevallos *et al.* investigated the use of a time-gate to suppress multiple scattering noise in a backscattered image [71]. The authors used both 130 fs and 3.5 ns laser pulses centered on 800 nm with an average beam power of 60 mW. For a time-gate, they used a fast-gated intensified camera system capable of generating shutter-times between 80 ps and 6 ns. The authors investigated the backscattered signal from a test chart placed in the center of a 100x100x50 mm^3 cuvette filled with 0.5 μm TiO_2 particles suspended in distilled water. Their results showed that the short-pulse/short-gate combination (130 fs/80 ps) was the only combination capable of generating a visible backscattering image of the test chart. Using a time-gate with a shutter time $\sim$80 ps will, however, result in a depth-resolution of around 2.5 cm. When the intention is to probe the liquid core of modern DICI engine fuel sprays, such a depth-resolution would be insufficient.

Using the OKE based time-gate of BI, on the other hand, considerably shorter shutter times than 80 ps can be reached. The single-color crossed-beam OKE-gate, as an example, would correspond to a depth-resolution around 0.45 mm. Thus, time-gated backscattering based on the OKE-gate (*i.e.* TGS) could potentially provide images with a depth-resolution on the same order of magnitude as the dimensions of modern DICI engine fuel sprays. In Fig. 4.1, a schematic of a TGS setup using an OKE-gate is shown. This setup was used in Paper V, in an initial investigation of the TGS technique. In Chapter 5.2, further investigations of the TGS technique are presented. Here the use of a two-color collinear OKE-gate was investigated, and the setup was used to study the spray formation region of a water spray.

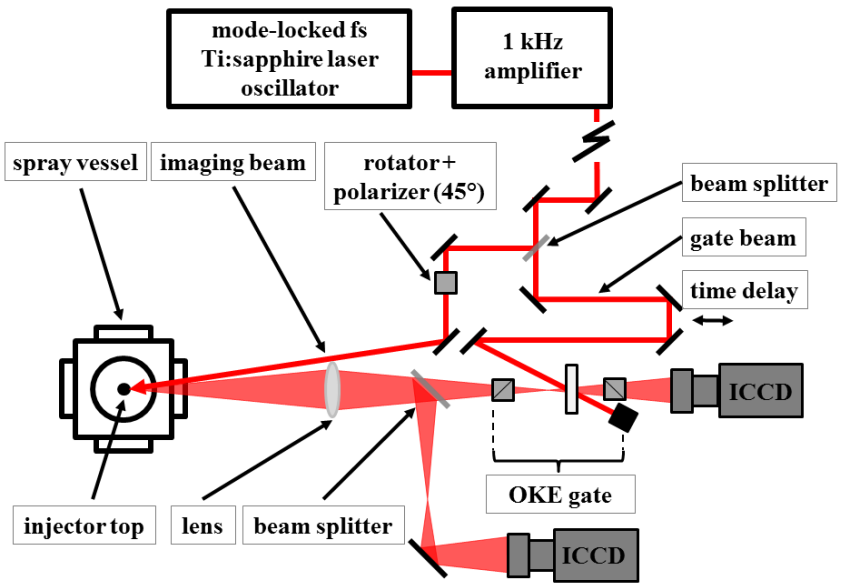

Figure 4.1: *Schematic of a TGS setup using a single-color crossed-beam OKE-gate.*

Chapter 5

Results

This Chapter provides a summary of the results obtained in the work constituting this thesis. In section 5.1 the published papers are summarized, and in section 5.2 unpublished work regarding the use of the collinear OKE-gate in a TGS setup is presented.

5.1 Published papers

Paper I

> **M. Rahm**, M. Paciaroni, Z. Wang, D. Sedarsky, and M. Linne, "Evaluation of optical arrangements for ballistic imaging in sprays", Optics Express **23**, 22444-22462 (2015).

In this paper, the 4*f* and 2*f* time-gated BI setups discussed in section 3.4 were investigated and compared. The investigation contained both experiments in scattering and in non-scattering environments, as well as computational model-

ing. A single-color crossed-beam geometry were used for an OKE-gate.

The experiments showed that, in terms of ultimate resolution, the two setups performed similarly in the presence of scatterers. In terms of contrast, the $2f$ setup performed better in the lower scatterer size range and in the densest cases. With larger scatterer sizes at moderate ODs, the results were mixed. The experiments further indicated that the $4f$ setup was more sensitive to system aberrations than the $2f$ setup.

To gain a better understanding of the sources of aberrations and the difference in sensitivity to them, a set of experiments combined with modeling were performed. It was shown that positioning of the Kerr medium along the optical axis is important since the image beam, when focused, could generate unwanted non-linear lensing effects. It was also shown that variations in the gate energy affect the two setups differently; the $4f$ setup is more sensitive to variations in the gate pulse energy than the $2f$ setup. An analytical investigation indicated that the gate pulse generates a focusing effect in the Kerr medium that induces image distortions. This focusing is a consequence of the spatial profile of the induced birefringence in the Kerr medium discussed in section 3.3.1. By modeling this lensing with a physical optics code, it was shown that both setups were affected by changes in the gate beam energy and by induced asymmetries introduced by moving the gate beam in the transverse direction. In the model, however, the $4f$ setup exhibited a more significant degradation in imaging performance as a result of these factors.

The investigations of the two different optical setups used in BI indicate that the $2f$ system is more robust to misalignment and, hence, more easily used. It is less prone to image distortions caused by component misalignments, changes in object plane position, and variations in the OKE-gate setup. The $2f$ time-gated BI setup was furthermore compared to its non-gated shadow-imaging equivalent in the same scattering conditions as the BI-setup comparison, in order to determine cases when the OKE-gate enhances imaging performance. Based on this investigation it was shown that the time-gated BI setup generated higher

contrast for most PS sphere sizes and ODs. In terms of resolution, it was only in the lower scatterer size range at low ODs that the non-gated shadow-imaging setup generated higher spatial resolution than the time-gated BI setup.

M. Paciaroni, M. Linne, and I planned the experiments. The experiments were set up and analyzed by M. Paciaroni, Z. Wang, and me. I performed the modeling of the optical setups. The manuscript was prepared by D. Sedarsky, M. Linne, and me.

Paper II

> D. Sedarsky, **M. Rahm**, and M. Linne, "Visualization of acceleration in multiphase fluid interactions", Optics Letters **41**, 1404-1407 (2016).

This paper is concerned with a 3-pulse BI system generating two-dimensional velocity and acceleration data for the liquid/gas interfaces in the spray formation region. Here a Ti:Sapphire oscillator seeded three regenerative amplifiers, each operating at a repetition rate of 1 kHz. Combination of the three amplifier output beams into a single beam generated a 1 kHz burst of pulse triplets. Intra-triplet pulse spacing was controlled by the timing of the amplifier pump lasers, thereby enabling pulse spacing down to $\sim$12 ns. After beam combination, the pulse train was split into image and gate parts, and the spray images were generated with a BI setup using a crossed-beam OKE-gate geometry. The BI image triplet (I_1-I_3) was recorded with two intensified interline-transfer cameras (Princeton PI-MAX4 ICCD), and correlated spatially using a static grid target.

From the image triplet, two sets of velocity correlations (V_1 and V_2) could be calculated. Initially, a set of target regions were defined for I_1 and their displacement in I_2 were calculated using normalized cross-correlations, resulting in V_1. The coordinates for the matched regions in I_2 were subsequently used as target regions in the correlation between I_2 and I_3, resulting in V_2. By differ-

encing V_2 and V_1, the mean acceleration between I_1 and I_3 could be inferred.

This setup was used to study a turbulent water jet issuing into atmospheric conditions. The water was injected with an injection pressure of 19 bar through a plain-orifice nozzle with a length/diameter ratio of 25. The images were captured 28 mm below the nozzle. For this experiment, an intra-frame spacing of 10 μs was suitable; it provided sufficient structure displacement without compromising correlation strength due to excessive structure deformation. The velocity results for the investigated spray indicated, as expected, motion predominantly taking place in the streamwise direction, with a radially decreasing velocity profile. The median axial velocity was 37 m/s. The acceleration correlation indicated that the liquid structures were subjected to an overall acceleration in the positive radial direction coupled with a retardation in the streamwise direction. This indicates that both turbulence and shear forces were affecting the breakup of the liquid jet. The median radial acceleration was 2.6 m/s^2 and the median axial deceleration was 1.7 m/s^2.

The experiments were planned by D. Sedarsky, M. Linne, and me. I designed the optical setup and acquired the data. Image processing and code development were done by D. Sedarsky. The manuscript was prepared by D. Sedarsky, M. Linne, and me.

Paper III

> Z. Falgout, **M. Rahm**, Z. Wang, and M. Linne, "Evidence for supercritical mixing layers in the ECN Spray A", Proceedings of the Combustion Institute **35**, 1579-1586 (2015).

In this paper, a dodecane spray from a single-hole Bosch injector with an 84 μm ECN nozzle was investigated [72]. The spray was injected with 1500 bar pressure into an ambient gas with elevated pressures and temperatures. This was the first time time-gated BI was used to investigate a fuel spray at DICI

engine-relevant pressures and temperatures. The steady flow spray chamber at Chalmers University of Technology was used to generate two different test cases, one being a low temperature case (LTC) and the other being a high temperature case (HTC). The HTC correspond to the ECN spray A condition. For pure dodecane, the LTC condition corresponds to a thermodynamically subcritical state. The HTC condition, on the other hand, corresponds to a thermodynamically supercritical state.

These two conditions, the LTC and the HTC, are the same conditions that Dahms *et al.* argued to show a transition from a conventional two-phase spray to a transitionally supercritical case with a dense mixing layer [9]. Based on the findings in Paper I these conditions were investigated with a $2f$ BI setup. The sprays were investigated in the steady period and late in injection.

In the LTC, the findings indicated a conventional two-phase behavior of the spray, with a liquid core showing a sharp interface separating the liquid from the gas. Features like stripping of ligaments from the core could be seen. The images furthermore showed a core radius growing with downstream distance. Due to mass conservation of a core shedding ligaments and drops, this behavior could indicate a non-contiguous core with larger liquid structures separated by entrained gas.

In the HTC, the behavior of the dodecane spray changed. In the steady injection period, the images showed a dark core in the spray formation region, but the core edge was defined by a cellular structure. The cellular structure comes from light propagating through refractive index gradients caused by local density gradients, thus acting like a micro-lens array. The sharp two-phase interface from the LTC was replaced by a thickened mixing layer in the HTC. Late in injection, this cellular structure of the mixing layer was more emphasized, and the jet structure resembled structures seen in shadow-imaging of turbulent gas jets. Ligaments could not be seen either in the steady period or late in injection.

These findings show that a significant change in jet structure occurs for the dodecane spray when changing the conditions from a subcritical case to a super-

critical case for the pure liquid. However, transillumination imaging generates data based on refractive index changes in the probed region. These changes do not necessarily correspond directly to changes in the thermodynamic state. As a consequence, these findings are not fully conclusive, but they do not contradict the hypothesis that dodecane sprays can be transitionally supercritical at the ECN spray A condition.

Z. Falgout, Z. Wang, M. Linne, and I planned the experiments. Z. Falgout designed and assembled the injection system and adapted it to the spray rig. The ballistic imaging setup was designed and assembled by me. Z. Falgout, Z. Wang, and I performed the measurements. Z. Falgout and M. Linne analyzed the data and prepared the manuscript.

Paper IV

> Z. Falgout, **M. Rahm**, D. Sedarsky, and M. Linne, "Gas/fuel jet interfaces under high pressures and temperatures", Fuel **168**, 14-21 (2016).

The work presented in this paper is a continuation of the investigation of potential transient supercriticality discussed in Paper III. The sprays were investigated by simultaneously using both BI and non-gated shadow-imaging setups using the same femtosecond illumination source. These setups are similar to the gated and non-gated 2*f* setups discussed in Paper I.

The three pure fuels Butanol, n-hexadecane, n-dodecane (henceforth called hexadecane and dodecane), and a commercially available Diesel blend were investigated at three different chamber conditions (Cases 1-3). Based on an estimation of the thermodynamic properties of mixtures of the pure fuels and nitrogen, the cases were chosen to represent three different thermodynamic states. In Case 1, all three pure fuel mixtures were estimated to have critical temperatures (T_c) above the chamber temperature. In Case 2, the butanol and dodecane

mixtures had a T_c below the chamber temperature, while hexadecane mixtures were estimated to be subjected to subcritical conditions. Case 3 corresponded to a chamber temperature well above the estimated T_c for all pure fuel mixtures. That is, for the pure fuels, the three cases spanned a region from subcritical to supercritical conditions via an intermediate case.

When investigating the three pure fuels, a clear change in image morphology could be seen. In Case 1 where all fuel mixtures have T_c well above the chamber temperature, both BI and the non-gated images indicated the jets to be in an atomizing spray regime. With BI, one could see a distinct liquid/gas interface, and the non-gated images showed the presence of a drop cloud. In Case 2, the images started to change. For butanol and dodecane, which both had T_c below the chamber temperature, BI showed a beginning of the cellular structures discussed in Paper III. These cellular structures in BI indicate a transition from the distinct two-phase interface to a thickened mixing layer dominated by refractive index changes caused by local density gradients. Hexadecane did not exhibit these structures. For hexadecane in case 2, BI showed structures attributed to a normal atomizing spray. In Case 3, the chamber temperature was above T_c for all pure fuels. With BI, all three fuels showed the cellular structures. Hexadecane however, to a lesser degree than the others.

Diesel, which is a blend of many fuel components, was also investigated in the three cases. Since it is a multicomponent blend, its thermodynamic properties can be very different from the properties of the individual pure components. Estimation of its thermodynamic properties using the methodology used for the pure fuels was not possible. In the Diesel case, both BI and the non-gated images indicated a normal atomizing spray regime in Case 1 and Case 2. Only in Case 3, there was some evidence of a nascent cellular structure. Diesel was much less affected by the changes in pressure and temperature than the other investigated pure fuels.

The conclusion of the investigation is that for the pure fuels a change in spray structure, mostly coinciding with the supercritical parameters, could be

observed. In the Diesel case, on the other hand, a clear change in spray structure could not be observed in the evaluated cases. It appears, however, that if the Diesel jet is about to enter a different regime, the transition is just beginning in Case 3. However, as pointed out in the discussion regarding Paper III, transillumination imaging is not a technique for direct measurement of thermodynamic states. Rather, transillumination imaging generates data based on refractive index changes in the probed region, which do not necessarily correlate with changes in thermodynamic state.

Z. Falgout, D. Sedarsky, M. Linne, and I planned the experiments. Z. Falgout designed and assembled the injection system and adapted it to the spray rig. Z. Falgout conducted the thermodynamic analysis. Z. Falgout and I designed and assembled the ballistic imaging setup. The measurements were performed by Z. Falgout and me. Z. Falgout, D. Sedarsky, and M. Linne analyzed the data and prepared the manuscript.

Paper V

> **M. Rahm**, Z. Falgout, D. Sedarsky, and M. Linne, "Optical sectioning for measurements in transient sprays", Optics Express **24**, 4610-4621 (2016).

This paper is concerned with an initial investigation of the TGS technique. As discussed in Chapter 4, this approach can potentially provide additional depth-resolved information regarding the liquid core of highly atomizing sprays.

The backscattered light signal was split in two parts, one directed directly to a camera and the other through a crossed-beam OKE-gate before reaching the camera. In this way, simultaneous non-TGS and TGS images could be captured and compared. The viability of the time-gated backscattering approach was initially investigated by illuminating a ground glass tube with a wall thickness of 0.75 mm. By adjusting the OPL of the gate beam, the OKE-gate could

be stepped through the backscattered image signal. In this way, scattering contributions from the different glass tube interfaces could be distinguished. This experiment showed the ability of the setup to generate depth-resolved images.

The setup was further applied to Diesel and dodecane sprays injected into the Chalmers steady flow spray chamber with 1500 bar. Two different chamber conditions were investigated, one being a low pressure-low temperature condition (LP-LT) and the other being a high pressure-high temperature condition (HP-HT). These two conditions are the same conditions investigated for a potential thermodynamic phase transition in Paper IV (Case 1 and Case 3). In the LP-LT condition with a Diesel spray, the generated non-TGS images contained high intensity structures near the nozzle. A few of these intensity structures, which likely come from reflections from larger fluid structures, are shown with high visibility in the corresponding TGS image. The reason is the OKE-gate, which selectively transmits light arriving at the gate at a specific time. In this way, scattering from a specific depth in the spray is detected. A trend in the Diesel HP-HT case (both non-time-gated and time-gated) was that high intensity structures, attributed to scattering from larger liquid structures, were seen less frequently than in the LP-LT case. This is likely an effect of the change in the chamber condition, which causes the spray to break up more vigorously. In the HP-HT condition, one could furthermore see effects of refractive index gradients in the gas that surround the spray. The refractive index gradients steer the light as it propagates the chamber and can affect the apparent spray position. Because the time-gate sample light scattered from a specific depth and not the complete signal, these image effects are reduced in the TGS image.

The experimental images contain glare spots, which are unavoidable when detecting backscattered light from transparent liquid structures and drops. Due to this, the technique cannot reliably be used for quantitative drop sizing. It can however, potentially reveal depth-resolved qualitative information about liquid structures in the spray formation region.

D. Sedarsky, M. Linne, and I planned the experiments. Z. Falgout designed and assembled the injection system and adapted it to the spray rig. I designed and assembled the TGS setup. I performed the measurements and post-processing of the data. D. Sedarsky, M. Linne, and I analyzed the data and prepared the manuscript.

5.2 Unpublished findings

5.2.1 Collinear OKE-gate

The collinear OKE-gate in Chapter 3.3.3 was investigated as a potential time-gate to be used in a TGS setup (discussed in Chapter 4 and in Paper V). The gate was proposed as a way to obtain shorter gates than the ones possible using the crossed-beam geometry. The use of a shorter gate in TGS would directly correspond to an increased depth-resolution of the technique.

The simple on-axis model of the induced refractive index in Eq. 3.4 can be used to improve understanding of the gating characteristics in the collinear geometry. Propagating the refractive index profile through the CS_2 with a velocity of $c/n_{800\text{nm}}$, and the image pulse with a velocity of $c/n_{400\text{nm}}$, the acquired phase difference between the two components of the image pulse can be calculated. The transmitted signal through the OKE-gate can then be calculated with Eq. 3.3. By varying the initial time delay between the image and gate pulses, the temporal behavior of the gate can be obtained. In Fig. 5.1, modeled gate profiles for CS_2 path lengths of 1 mm, 3 mm, 6 mm, and 10 mm are shown. Here the gate pulse was assumed to have a Gaussian temporal profile with a 100 fs pulse length (FWHM), thus inducing the refractive index profile shown in Fig. 3.2. For simplicity, the image pulse was modeled as a delta function. In Fig. 5.1, the effect of the CS_2 path length is clear. The calculated gate lengths (FWHM) for the 1 mm, 3 mm, 6 mm, and 10 mm CS_2 path lengths were 1.2 ps, 3.0 ps, 6.5 ps, and 11.3 ps respectively; which is in good agreement with the

experimental results of Purwar *et al.* [64]. The thickness of the Kerr cell places constraints on the range of initial time delays able to result in a polarization rotation of the image pulse.

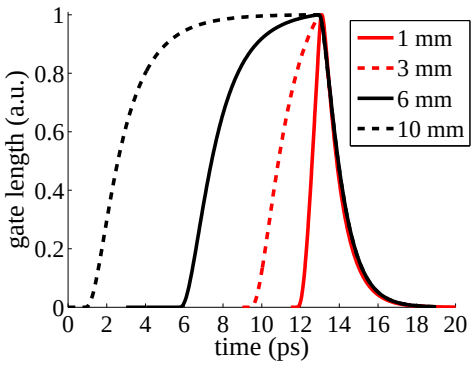

Figure 5.1: *Temporal behavior of the on-axis two-color collinear OKE-gate model as a function of CS_2 path length. All gate profiles are normalized to one. The gate lengths for the 1 mm, 3 mm, 6 mm, and 10 mm CS_2 path lengths are 1.2 ps, 3.0 ps, 6.5 ps, and 11.3 ps respectively.*

The collinear gate was further investigated experimentally. A schematic of the experimental setup is shown in Fig. 5.2. Here a mode-locked Ti:Sapphire oscillator seeded two chirped-pulse regenerative amplifiers with ∼80 fs pulses (FWHM) centered on 800 nm. The output from each amplifier was a 1 kHz pulse train of ∼100 fs pulses (FWHM) with a beam diameter of ∼8 mm ($1/e^2$). The optical energy per pulse was ∼4 mJ. Two amplifiers were used since high image pulse energies as well as good gating efficiencies are required for TGS to be functional. The collinear OKE-gate requires high gate pulse energies to give good gating efficiencies, and high energy of the image pulses are needed to overcome the losses in the SHG conversion. The output from amplifier 1 was used as the source light for the image pulses. The image beam was routed through a BBO-crystal to generate pulses centered on 400 nm before illuminating the object. The non-converted part of the image beam was blocked with

a shortpass filter. The image was collected with an achromatic lens with a 200 mm focal length. After the collecting lens, the image pulse was divided into two parts, time-gated and non-time-gated parts, using a beamsplitter. The time-gated part was passed through the collinear OKE-gate, placed in a Fourier-plane, and then recorded with an EMCCD camera. The non-time-gated part was directed straight to an EMCCD camera. The OKE-gate consisted of a Kerr medium surrounded by two polarizers. CS_2 was used as the Kerr medium, and placed in a 1 mm thick cell with a clear aperture of 40 mm. The polarizers were 15x15 mm^2 Glan-Laser Calcite polarizers with extinction ratio of 10^5:1. The output from amplifier 2 was used as the source light for the gate pulses. The gate beam had its polarization rotated 45° with respect to the polarization of the image beam, and was combined with the image beam after the first OKE-gate polarizer using a dichroic mirror. After the CS_2-cell, the gate beam was blocked with a shortpass filter with a suppression ratio of more than 10^5:1 in the rejection region. Both the image and gate beams had computer controlled retro-reflecting time-delays (TD1 and TD2) to control the optical path length of each beam. Synchronization of the amplifiers combined with the time-delay stages ensured control of temporal overlap of the image and gate pulses inside the CS_2-cell.

In Fig. 5.3, a gate trace from the experimental setup is shown. Here the gate pulse energy was 2.3 mJ and the resulting gate length was 1.0 ps (FWHM). To investigate how the gate efficiency scaled with the gate pulse energy, a set of measurements were conducted with gate pulse energies ranging from 0.75 mJ to 2.25 mJ. The results can be seen in Fig. 5.4. The experimental data are shown together with results from gate efficiency calculations using the on-axis model with a 1 mm thick CS_2-cell. As can be seen, the experiments and the model show similar trends with respect to gate pulse energies. However, the experimentally measured efficiencies are consistently lower than the efficiencies predicted by the model. In part, this is an effect of the model only using light on the optical axis in the estimation of the efficiency. That is, only light experiencing maximum polarization rotation is used.

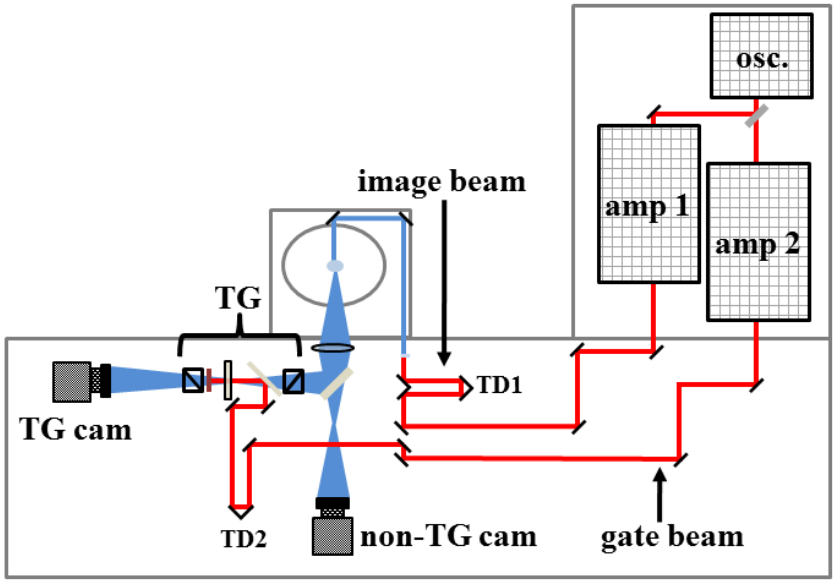

Figure 5.2: *Schematic of the experimental two-color collinear BI setup.*

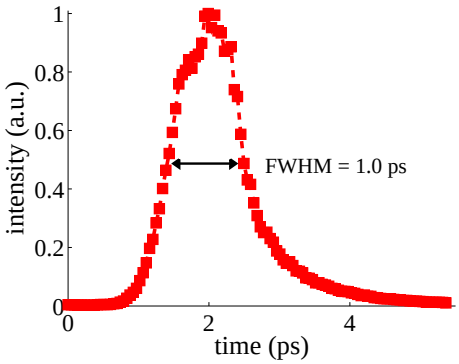

Figure 5.3: *Experimentally measured transmission through the two-color collinear OKE-gate. A 1 mm CS_2 cell was used as the Kerr medium, and the gate pulse energy was 2.3 mJ. The measured gate length was 1.0 ps (FWHM).*

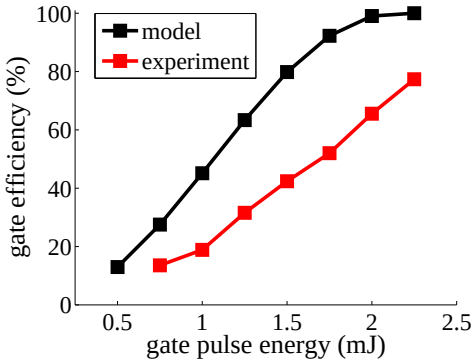

Figure 5.4: *Experimentally measured gate efficiencies for the two-color collinear OKE-gate shown together with the results predicted by the on-axis model. The gate pulse energy was varied between 0.75 mJ and 2.25 mJ. The corresponding experimentally measured efficiencies increased from 15% to 75%.*

From the investigation, it was concluded that using the two-color collinear OKE-gate with a 1 mm path length CS_2-cell is a good alternative for a TGS setup with a shorter time-gate than possible in a single-color crossed-beam configuration. However, the setup requires comparatively high gate pulse energies to get sufficiently high gate efficiencies. Combining this energy requirement with the losses in the SHG conversion and the TGS need for high image pulse energies, care must be taken to ensure availability of sufficient levels of optical energy.

5.2.2 Time-gated sectioning

The collinear OKE-gate was subsequently tested in a TGS setup. The setup shown in Fig. 5.2 was modified to give a backscattering geometry. In this geometry, the angle between the image beam and the optical axis of the imaging setup was $\sim 12^\circ$.

Initially a TGS scan of the backscatter signal from the ground glass tube used in Paper V was performed to investigate the sectioning capabilities of this new setup. Figure 5.5 shows a photograph of the glass tube together with its dimensions, and Fig. 5.6 shows the resulting time-gated backscatter signal. In this experiment the gate pulse energy was 2 mJ, which gave a gate efficiency of around 65% and a gate length of 1.0 ps (resulting in a depth-resolution of $\sim$0.3 mm). In the signal in Fig. 5.6, contributions from all four glass tube surfaces can be seen. Comparing these results to the scan shown in Paper V (Fig. 4), it can be seen that more details can be identified than in the original crossed-beam setup. This is both due to more energy in the image pulses, and to the increased depth-resolution of the collinear gate.

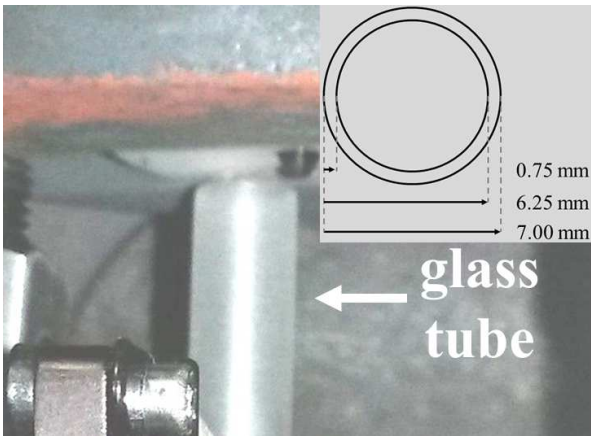

Figure 5.5: *Photo of the ground glass tube used for optical sectioning characterization. Dimensions of the tube are indicated in the inset.*

The collinear TGS setup was further applied to a water spray. The spray was formed using an injection pressure of 24 bar and a plain-orifice nozzle with a diameter of 6 mm. The images were captured 30 mm below the nozzle, and the OKE-gate was activated with gate pulse energies of 2 mJ.

Figure 5.7 contains simultaneous TGS and non-TGS (not time-gated) im-

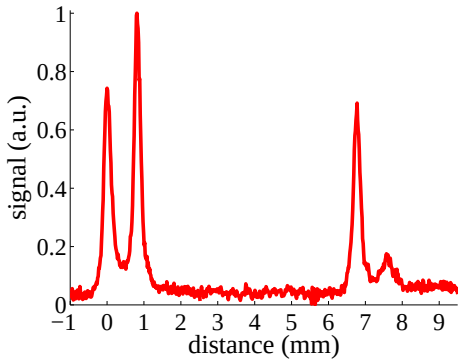

Figure 5.6: *Experimentally measured scan through the backscattered signal from the ground glass tube. Here gate pulse energies of 2 mJ was used to activate the OKE-gate.*

ages of the spray formation region in a case where the OKE-gate was set to accept light scattered close to the center of the spray. Interpretation of the non-TGS image is difficult due to high intensity scattering from across the field of view. The TGS image, on the other hand, shows what appears to be scattering from a larger liquid structure. The image of the structure is fragmented and there is evidence of glare spots. As argued in Paper V, contributions from glare spots are unavoidable when using backscattered light from transmissive structures. The fragmented appearance of the structure could, however, be partly due to sampling of light from a planar section thinner than the thickness of the liquid structure. That is, part of the fragmentation could be due to the wrinkled nature of the turbulent liquid surface. Therefore, one way to improve the technique could be to harmonize the sampling depth with the thickness of the imaged structures. As shown in Fig. 5.1, a tuning of the depth-resolution could be achieved by carefully adjusting the thickness of the Kerr medium.

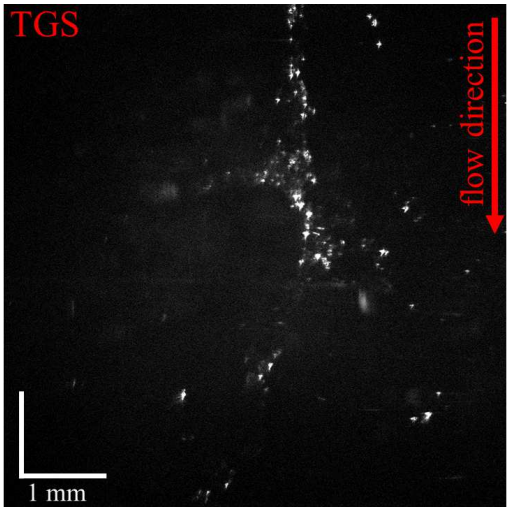

(a) TGS image.

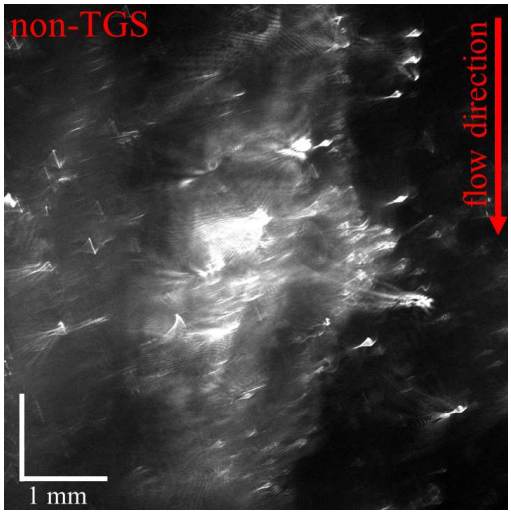

(b) Non-TGS image.

Figure 5.7: *Simultaneous TGS and non-TGS (not time-gated) images of a water spray issued with a 24 bar injection pressure and a nozzle diameter of 6 mm. The images were captured 30 mm below the nozzle.*

Chapter 6

Concluding remarks

The work presented in this thesis provides further insight into the use of time-gated imaging techniques for spray studies. The work covers both method development and application of the techniques to industrially relevant sprays.

The comparison of the two BI setups previously used for spray investigations showed that the simpler $2f$ setup is more robust to component misalignment and less affected by changes in the time-gate setup than the $4f$. During the investigation it was also noted that the time-gate itself had a significant effect on the generated images. This issue was investigated in more detail, and it was shown that the time-gate can have a lensing effect that introduces image aberrations. We conclude that the $2f$ setup is often preferable for spray investigations.

The velocity-BI technique was further improved with the addition of a third laser amplifier. Thereby both velocity and acceleration of larger liquid structures in the spray formation region could be acquired. This is an important development since the generated information can be used to estimate the effects of the forces causing the breakup. Future work on velocity and acceleration-BI should focus on generating accurate velocity and acceleration data sets for

sprays relevant to code development.

In an applied investigation, the BI technique was for the first time used to study fuel sprays at engine-relevant pressures and temperatures. Here the ambient conditions were varied and changes in the liquid/gas interfaces in the spray formation region were studied. It was shown that especially for single-component fuels the liquid/gas interfaces exhibited a significant change, which mostly correlated with the thermodynamic properties of the fuels. For the Diesel blend, the changes in the interface were less significant in the investigated conditions. The observed changes for the pure fuels may indicate a transition to a supercritical regime.

The investigation of the fuel sprays indicated the existence of a liquid core that increased radially in the downstream direction. To gain further understanding on this issue a technique capable of generating depth-resolved images of the spray formation region must be employed. To this end time-gated sectioning was investigated as a potential candidate. This setup captures backscattered light from the spray formation region, and was successfully able to generate a depth-resolution of $\sim$0.3 mm The TGS technique is, however, still at an initial stage. The generated images cannot be fully interpreted, and the maximum penetrable optical depth is not known. Future work should aim to shed light on these issues. A better understanding of backscatter images of wrinkled and transmissive structures illuminated with initially coherent light is vital for accurate interpretation of the TGS images of the spray formation region.

Taken together, the work constituting this thesis improves time-gated imaging techniques for studies of the spray formation region, as well as contributes to the understanding of fuel sprays under engine-relevant pressures and temperatures. Improved methods for investigation, and thereby a deeper understanding, of the processes causing the breakup of fuel sprays are vital for the development of the high-efficiency/low-emission engines needed for future sustainable transportation.

Bibliography

[1] S. Chu and A. Majumdar, "Opportunities and challenges for a sustainable energy future," Nature **488**, 294–303 (2012).

[2] M. Fischer, M. Werber, and P. V. Schwartz, "Batteries: Higher energy density than gasoline?" Energ. Policy **37**, 2639–2641 (2009).

[3] S. Chu, "The science of photons to fuel," AIP Conference Proceedings **1044**, 266–282 (2008).

[4] R. Pachauri and L. Meyer (editors), "Climate change 2014: Synthesis report. contribution of working groups i, ii and iii to the fifth assessment report of the intergovernmental panel on climate change," IPCC, Geneva, Switzerland (2014).

[5] J. Dec, "A conceptual model of DI diesel combustion based on laser-sheet imaging," In: SAE technical paper series, paper no. 970873 (1997).

[6] D. P. Schmidt and M. L. Corradini, "The internal flow of diesel fuel injector nozzles- a review," Int. J. Engine Res. **2**, 1–22 (2001).

[7] M. Blessing, G. König, C. Krüger, U. Michels, and V. Schwarz, "Analysis of flow and cavitation phenomena in diesel injection nozzles and its effects on spray and mixture formation," In: SAE technical paper series, paper no. 2003-01-1358 (2003).

[8] M. Linne, "Imaging in the optically dense regions of a spray: A review of developing techniques," Prog. Energy Combust. Sci. **39**, 403–440 (2013).

[9] R. N. Dahms, J. Manin, L. M. Pickett, and J. C. Oefelein, "Understanding high-pressure gas-liquid interface phenomena in diesel engines," P. Combust. Inst. **34**, 1667–1675 (2013).

[10] R. N. Dahms and J. C. Oefelein, "On the transition between two-phase and single-phase interface dynamics in multicomponent fluids at supercritical pressures," Phys. Fluids **25**, – (2013).

[11] J. Oefelein, G. Lacaze, R. Dahms, A. Ruiz, and A. Misdariis, "Effects of real-fluid thermodynamics on high-pressure fuel injection processes," SAE Int. J. Engines **7**, 1125–1136 (2014). 2014-01-1429.

[12] R. N. Dahms and J. C. Oefelein, "Non-equilibrium gas-liquid interface dynamics in high-pressure liquid injection systems," P. Combust. Inst. **35**, 1587–1594 (2015).

[13] L. Qiu and R. D. Reitz, "Simulation of supercritical fuel injection with condensation," Int. J. Heat Mass Tran. **79**, 1070–1086 (2014).

[14] L. Qiu and R. D. Reitz, "An investigation of thermodynamic states during high-pressure fuel injection using equilibrium thermodynamics," Int. J. Multiphas. Flow **72**, 24–38 (2015).

[15] C. F. Bohren and D. R. Huffman, *Absorption and scattering of Light by Small Particles* (John Wiley & Sons, Inc, 1983).

[16] J. A. Lock and L. Yang, "Interference between diffraction and transmission in the Mie extinction efficiency," J. Opt. Soc. Am. A **8**, 1132–1134 (1991).

[17] N. E. Tayali and C. J. Bates, "Particle sizing techniques in multiphase flows: A review," Flow Meas. Instrum. **1**, 77–105 (1990).

[18] C. Roze, T. Girasole, L. Mees, G. Grehan, L. Hespel, and A. Delfour, "Interaction between ultra short pulses and a dense scattering medium by monte carlo simulation: consideration of particle size effect," Opt. Commun. **220**, 237–245 (2003).

[19] E. Berrocal, "Multiple scattering of light in optical diagnostics of dense sprays and other complex turbid media." Ph.D. thesis, School of Engineering, Cranfield University, Cranfield, UK (2006).

[20] C. Calba, L. Mees, C. Roze, and T. Girasole, "Ultrashort pulse propagation through a strongly scattering medium: simulation and experiments," J. Opt. Soc. Am. A **25**, 1541–1550 (2008).

[21] J. B. Blaisot and J. Yon, "Droplet size and morphology characterization for dense sprays by image processing-application to the diesel spray," Exp. Fluids **39**, 977–994 (2005).

[22] J. Labs and T. Parker, "Diesel fuel spray droplet sizes and volume fractions from the region 25 mm below the orifice," Atomization Spray **13**, 18 (2003).

[23] J. E. Labs and T. E. Parker, "Multiple-scattering effects on infrared scattering measurements used to characterize droplet size and volume fraction distributions in diesel sprays," Appl. Opt. **44**, 6049–6057 (2005).

[24] E. Berrocal, D. L. Sedarsky, M. E. Paciaroni, I. V. Meglinski, and M. A. Linne, "Laser light scattering in turbid media part i: Experimental and simulated results for the spatial intensity distribution," Opt. Express **15**, 10649–10665 (2007).

[25] E. Berrocal, D. L. Sedarsky, M. E. Paciaroni, I. V. Meglinski, and M. A. Linne, "Laser light scattering in turbid media part ii: Spatial and temporal analysis of individual scattering orders via monte carlo simulation," Opt. Express **17**, 13792–13809 (2009).

[26] A. Coghe and G. E. Cossali, "Quantitative optical techniques for dense sprays investigation: A survey," Opt. Laser Eng. **50**, 46–56 (2012).

[27] T. Fansler and S. Parrish, "Spray measurement technology: a review," Meas. Sci. Technol. **26**, 012002 (2015).

[28] M. Neil, R. Juskaitis, and T. Wilson, "Method of obtaining optical sectioning by using structured light in a conventional microscope," Opt. Lett. **22**, 1905–1907 (1997).

[29] T. Breuninger, K. Greger, and E. H. K. Stelzer, "Lateral modulation boosts image quality in single plane illumination fluorescence microscopy," Opt. Lett. **32**, 1938–1940 (2007).

[30] E. Kristensson, E. Berrocal, M. Richter, S.-G. Pettersson, and M. Alden, "High-speed structured planar laser illumination for contrast improvement of two-phase flow images," Opt. Lett. **33**, 2752–2754 (2008).

[31] E. Berrocal, E. Kristensson, M. Richter, M. Linne, and M. Alden, "Application of structured illumination for multiple scattering suppression in planar laser imaging of dense sprays," Opt. Express **16**, 17870–17881 (2008).

[32] E. Kristensson, L. Araneo, E. Berrocal, J. Manin, M. Richter, M. Alden, and M. Linne, "Analysis of multiple scattering suppression using structured laser illumination planar imaging in scattering and fluorescing media," Opt. Express **19**, 13647–13663 (2011).

[33] E. Berrocal, E. Kristensson, P. Hottenbach, M. Alden, and G. Grunefeld, "Quantitative imaging of a non-combusting diesel spray using structured laser illumination planar imaging," Appl. Phys. B **109**, 683–694 (2012).

[34] R. Domann and Y. Hardalupas, "Quantitative measurement of planar droplet sauter mean diameter in sprays using planar droplet sizing," Part. Part. Syst. Char. **20**, 209–218 (2003).

[35] Y. N. Mishra, E. Kristensson, and E. Berrocal, "Reliable LIF/Mie droplet sizing in sprays using structured laser illumination planar imaging," Opt. Express **22**, 4480–4492 (2014).

[36] C. Chartier, J. Sjöholm, E. Kristensson, O. Andersson, M. Richter, B. Johansson, and M. Alden, "Air-entrainment in wall-jets using SLIPI in a heavy-duty diesel engine," SAE Int. J. Engines **5**, 1684–1692 (2012). 2012-01-1718.

[37] E. Kristensson, M. Richter, and M. Alden, "Nanosecond structured laser illumination planar imaging for single-shot imaging of dense sprays," Atomization Spray **20** (2010).

[38] E. Kristensson, E. Berrocal, and M. Alden, "Two-pulse structured illumination imaging," Opt. Lett. **39**, 2584–2587 (2014).

[39] D. Duke, A. Swantek, N. Sovis, F. Tilocco, C. Powell, A. L. Kastengren, D. Gürsoy, and T. Bicer, "Time-resolved x-ray tomography of gasoline direct injection sprays," SAE Int. J. Engines **9** (2015).

[40] B. R. Halls, T. R. Meyer, and A. L. Kastengren, "Quantitative measurement of binary liquid distributions using multiple-tracer x-ray fluorescence and radiography," Opt. Express **23**, 1730–1739 (2015).

[41] A. Bravin, "Exploiting the x-ray refraction contrastwith an analyser: the state of the art," J. Phys. D Appl. Phys. (2003).

[42] C. D. Radke, J. Patrick McManamen, A. L. Kastengren, B. R. Halls, and T. R. Meyer, "Quantitative time-averaged gas and liquid distributions using x-ray fluorescence and radiography in atomizing sprays," Opt. Lett. **40**, 2029–2032 (2015).

[43] L. M. Pickett, J. Manin, A. Kastengren, and C. Powell, "Comparison of near-field structure and growth of a diesel spray using light-based optical microscopy and x-ray radiography," SAE Int. J. Engines **7**, 1044–1053 (2014). 2014-01-1412.

[44] R. R. Alfano, S. G. Demos, P. Galland, S. K. Gayen, Y. Guo, P. P. Ho, X. Liang, F. Liu, L. Wang, Q. Z. Wang, and W. B. Wang, "Time-resolved and nonlinear optical imaging for medical applications," Ann. NY. Acad. Sc. **838**, 14–28 (1998).

[45] M. Paciaroni and M. Linne, "Single-shot, two-dimensional ballistic imaging through scattering media," Appl. Opt. **43**, 5100–5109 (2004).

[46] M. Linne, M. Paciaroni, J. Gord, and T. Meyer, "Ballistic imaging of the liquid core for a steady jet in crossflow," Appl. Opt. **44**, 6627–6634 (2005).

[47] M. Linne, D. Sedarsky, T. Meyer, J. Gord, and C. Carter, "Ballistic imaging in the near-field of an effervescent spray," Exp. Fluids **49**, 911–923 (2010).

[48] J. B. Schmidt, Z. D. Schaefer, T. R. Meyer, S. Roy, S. A. Danczyk, and J. R. Gord, "Ultrafast time-gated ballistic-photon imaging and shadowgraphy in optically dense rocket sprays," Appl. Opt. **48**, B137–B144 (2009).

[49] M. Linne, M. Paciaroni, T. Hall, and T. Parker, "Ballistic imaging of the near field in a diesel spray," Exp. Fluids **40**, 836–846 (2006).

[50] S. Idlahcen, C. Roze, L. Mees, T. Girasole, and J. B. Blaisot, "Sub-picosecond ballistic imaging of a liquid jet," Exp. Fluids **52**, 289–298 (2012).

[51] S. Duran, J. Porter, and T. Parker, "Ballistic imaging of sprays at diesel relevant conditions," In: ICLASS 2012, 12th International Conference on Liquid Atomization and Spray Systems (2012).

[52] D. L. Sedarsky, M. E. Paciaroni, M. A. Linne, J. R. Gord, and T. R. Meyer, "Velocity imaging for the liquid-gas interface in the near field of an atomizing spray: proof of concept," Opt. Lett. **31**, 906–908 (2006).

[53] D. Sedarsky, J. Gord, C. Carter, T. Meyer, and M. Linne, "Fast-framing ballistic imaging of velocity in an aerated spray," Opt. Lett. **34**, 2748–2750 (2009).

[54] A. Kuditcher, B. G. Hoover, M. P. Hehlen, E. N. Leith, S. C. Rand, and M. P. Shih, "Ultrafast, cross-correlated harmonic imaging through scattering media," Appl. Opt. **40**, 45–51 (2001).

[55] S. Farsiu, J. Christofferson, B. Eriksson, P. Milanfar, B. Friedlander, A. Shakouri, and R. Nowak, "Statistical detection and imaging of objects hidden in turbid media using ballistic photons," Appl. Opt. **46**, 5805–5822 (2007).

[56] L. Wang, P. P. Ho, C. Liu, G. Zhang, and R. R. Alfano, "Ballistic 2-D imaging through scattering walls using an ultrafast optical Kerr gate," Science **253**, 769–771 (1991).

[57] X. Liang, L. Wang, P. P. Ho, and R. R. Alfano, "Two-dimensional Kerr-fourier imaging of translucent phantoms in thick turbid media," Appl. Opt. **34**, 3463–3467 (1995).

[58] B. E. A. Saleh and M. C. Teich, *Fundamentals of Photonics 2nd ed.* (John Wiley Sons, Inc., 2007).

[59] D. Milam, "Review and assessment of measured values of the nonlinear refractive-index coefficient of fused silica," Appl. Opt. **37**, 546–550 (1998).

[60] R. A. Ganeev, A. I. Ryasnyansky, M. Baba, M. Suzuki, N. Ishizawa, M. Turu, S. Sakakibara, and H. Kuroda, "Nonlinear refraction in CS_2," Appl. Phys. B **78**, 433–438 (2004).

[61] D. McMorrow, W. T. Lotshaw, and G. A. Kenney-Wallace, "Femtosecond optical Kerr studies on the origin of the nonlinear responses in simple liquids," IEEE J. Quantum Elect. **24**, 443–454 (1988).

[62] I. A. Heisler, "Time-resolved optical Kerr-effect investigation on CS_2/polystyrene mixtures," J. Chem. Phys. **123**, 054509 (2005).

[63] S. Idlahcen, L. Mees, C. Roze, T. Girasole, and J. B. Blaisot, "Time gate, optical layout, and wavelength effects on ballistic imaging," J. Opt. Soc. Am. A **26**, 1995–2004 (2009).

[64] H. Purwar, S. Idlahcen, C. Roze, D. Sedarsky, and J. B. Blaisot, "Collinear, two-color optical Kerr effect shutter for ultrafast time-resolved imaging," Opt. Express **22**, 15778–15790 (2014).

[65] A. Samoc, "Dispersion of refractive properties of solvents: Chloroform, toluene, benzene, and carbon disulfide in ultraviolet, visible, and near-infrared," J. Appl. Phys. **94**, 6167–6174 (2003).

[66] D. Sedarsky, E. Berrocal, and M. Linne, "Quantitative image contrast enhancement in time-gated transillumination of scattering media," Opt. Express **19**, 1866–1883 (2011).

[67] A. Kastengren, C. F. Powell, Z. Liu, S. Moon, J. Gao, X. Zhang, and J. Wang, "Axial development of diesel sprays at varying ambient density," In: Proceedings of the 22nd annual conference on liquid atomization and spray systems (2010).

[68] A. G. Podoleanu, "Optical coherence tomography," J. Microsc. **247**, 209–219 (2012).

[69] S. Demos, H. Radousky, and R. Alfano, "Deep subsurface imaging in tissues using spectral and polarization filtering," Opt. Express **7**, 23–28 (2000).

[70] S. A. Kartazayeva, X. Ni, and R. R. Alfano, "Backscattering target detection in a turbid medium by use of circularly and linearly polarized light," Opt. Lett. **30**, 1168–1170 (2005).

[71] M. E. Zevallos L., S. K. Gayen, M. Alrubaiee, and R. R. Alfano, "Time-gated backscattered ballistic light imaging of objects in turbid water," Appl. Phys. Lett. **86**, 011115 (2005).

[72] L. M. Pickett, C. L. Genzale, G. Bruneaux, L.-M. Malbec, L. Hermant, C. Christiansen, and J. Schramm, "Comparison of diesel spray combustion in different high-temperature, high-pressure facilities," SAE Int. J. Engines **3**, 156–181 (2010). 2010-01-2106.